STRESS INTENSITY FACTOR ANALYSIS OF A THREE-DIMENSIONAL INTERFACE CRACK BETWEEN DISSIMILAR ANISOTROPIC MATERIALS UNDER THERMAL STRESS

Masaki Nagai[1], Toru Ikeda[1, *] and Noriyuki Miyazaki[1]

[1] *Department of Mechanical Engineering and Science, Kyoto University, Yoshida-Honmachi, Sakyo-ku, Kyoto 606-8501, Japan.*

* Corresponding author. Tel.:+81 75 753 5215; Fax: +81 75 753 5719
E-mail address: *ikeda@solid.me.kyoto-u.ac.jp*

Abstract

A numerical method for evaluating the stress intensity factors (SIFs) of a three-dimensional interface crack between dissimilar anisotropic materials subjected to thermal and mechanical stresses is proposed. The M_1-integral method was applied to an interfacial crack between three-dimensional anisotropic bimaterials under thermal stress. The moving least square approximation was utilized to calculate the value of the M_1-integral. The M_1-integral in conjunction with the moving least square approximation can be used to calculate the SIFs from nodal displacements obtained by finite element analysis. SIF analyses were performed for double edge cracks in jointed dissimilar isotropic semi-infinite plates subjected to thermal load. Excellent agreement was achieved between the numerical results obtained by the present method and the exact solution. In addition, we computed the SIFs of an external circular interfacial crack in jointed dissimilar anisotropic solids under thermal stress and showed the distributions of SIFs along the crack front. The distribution of stress and the crack opening displacement obtained by the asymptotic solution using the computed SIFs were compared with those obtained by the finite element analysis with fine mesh. They were almost identical to each other, except for the minor component of SIFs that is much smaller than the major component of SIFs. These results indirectly demonstrate the accuracy of the obtained SIFs.

Keywords: Stress intensity factor, Interfacial crack, Anisotropic material, Stroh formalism, M_1-integral, Moving least-square approximation, Thermal stress

1. Introduction

Electronic devices and micro-electro-mechanical systems (MEMS) are composed of many different materials and have many interfaces. The thermal stress resulting from the mismatch of the coefficient of thermal expansion between different materials often causes delamination along the interface. The delamination of the interface between different materials is one of the main causes of

the malfunction or the reliability degradation of electronic devices.

The stress intensity factors (SIFs) of an interface crack are important for evaluating the fracture at interfaces. Gotoh [1], Clements [2], Willis [3], Bassani and Qu [4], and Wu [5] have investigated the stress field around interfacial cracks between dissimilar anisotropic materials. Hwu [6] has proposed an asymptotic solution for stress around an interface crack between dissimilar anisotropic materials using the Stroh formalism [7], and defined the SIFs of an interface crack. Few analytical solutions of the SIFs of interface cracks between dissimilar anisotropic materials have been proposed due to the mathematical difficulty. The energy release rate of an interfacial crack can be obtained using an energy method such as the virtual crack extension method, the J-integral method or the crack closure integral method. Sun and Qian [8] and Ikeda et al. [9] proposed numerical methods to calculate the mode-separated SIFs of a two-dimensional interfacial crack between dissimilar anisotropic materials subjected to mechanical loads. Nagai et al. [10] and Nomura et al. [11] presented computational methods to determine the SIFs of a two-dimensional interfacial crack and corner between dissimilar anisotropic solids under thermal stress, respectively. Nagai et al. [12] proposed the modified M_1-integral method, which is a combination of the J-integral method and the superposition method, to obtain the SIFs of a three-dimensional crack between anisotropic bimaterials. However, there is still no numerical method based on the energy method to determine the SIFs of a three-dimensional interfacial crack between dissimilar anisotropic materials subjected to thermal stress.

We extended the M_1-integral to determine the SIFs of a three-dimensional interface crack between dissimilar anisotropic materials under thermal stress. In this method, the moving least-square approximation is employed to calculate the value of the M_1-integral, and the stress and strain in the M_1-integral are approximated from the nodal displacements obtained by the finite element analysis. Therefore, in the computation of the M_1-integral, this method does not need to extract any elemental data from the finite element analysis. The M_1-integral method presented here can calculate the SIFs easily and requires less time for the data preparation than other procedures.

2. Stress intensity factors of an interface crack between dissimilar anisotropic materials

The general solutions of an interface crack between dissimilar anisotropic materials, as shown in Figure 1, are expressed using the Stroh formalism [7].

$$
\begin{aligned}
\mathbf{u}_j &= \mathbf{A}_j \mathbf{f}_j(z) + \overline{\mathbf{A}_j \mathbf{f}_j(z)}, \\
\boldsymbol{\varphi}_j &= \mathbf{B}_j \mathbf{f}_j(z) + \overline{\mathbf{B}_j \mathbf{f}_j(z)}, \qquad \text{in Material } j.
\end{aligned}
\tag{1}
$$

where the overbar denotes the complex conjugate, and subscripts 1 and 2 indicate Material 1 ($x_2 >$

0) and Material 2 ($x_2 < 0$), respectively. $\mathbf{A}_j$ and $\mathbf{B}_j$ are 3 x 3 complex matrices composed of Stroh's eigenvectors for material j, which are calculated from the elastic stiffnesses (C_{ijks}) for Material j. $\mathbf{u}_j$ and $\boldsymbol{\varphi}_j$ are the displacement and stress function vectors in Material j, respectively.

$$\mathbf{u}_j = \begin{Bmatrix} u_1 \\ u_2 \\ u_3 \end{Bmatrix}, \quad \boldsymbol{\varphi}_{j,1} = \begin{Bmatrix} \varphi_{1,1} \\ \varphi_{2,1} \\ \varphi_{3,1} \end{Bmatrix} = \begin{Bmatrix} \sigma_{12} \\ \sigma_{22} \\ \sigma_{23} \end{Bmatrix}, \quad \boldsymbol{\varphi}_{j,2} = \begin{Bmatrix} \varphi_{1,2} \\ \varphi_{2,2} \\ \varphi_{3,2} \end{Bmatrix} = -\begin{Bmatrix} \sigma_{11} \\ \sigma_{12} \\ \sigma_{13} \end{Bmatrix}, \qquad \text{in Material } j. \tag{2}$$

Function vectors $\mathbf{f}_1(z)$ and $\mathbf{f}_2(z)$ are related to the function vector $\boldsymbol{\psi}(z)$ by the following formula:

$$\begin{aligned} \mathbf{f}_1(z) &= \mathbf{B}_1^{-1}\boldsymbol{\psi}(z) \\ \mathbf{f}_2(z) &= \mathbf{B}_2^{-1}\overline{\mathbf{M}}^{*-1}\mathbf{M}^*\boldsymbol{\psi}(z) \end{aligned}. \tag{3}$$

$\mathbf{M}^*$ is a bi-materials matrix obtained from the Barnett-Lothe tensors [13] of two materials as

$$\mathbf{M}^* = \mathbf{D} - i\mathbf{W} \tag{4}$$

$$\mathbf{D} = \mathbf{L}_1^{-1} + \mathbf{L}_2^{-1}, \quad \mathbf{W} = \mathbf{S}_1\mathbf{L}_1^{-1} - \mathbf{S}_2\mathbf{L}_2^{-1}, \tag{5}$$

where i is the complex number ($i^2 = -1$). Barnett-Lothe tensors $\mathbf{S}$ and $\mathbf{L}$ are obtained by

$$\mathbf{S} = \frac{1}{\pi}\int_0^\pi \mathbf{N}_1(\theta)d\theta, \quad \mathbf{L} = -\frac{1}{\pi}\int_0^\pi \mathbf{N}_3(\theta)d\theta. \tag{6}$$

$\mathbf{N}_1(\theta)$ and $\mathbf{N}_3(\theta)$ are the functions of the elastic constants of the respective materials.

Hwu [6] has defined the SIFs of an interface crack between dissimilar anisotropic materials which are compatible with those for a crack in a homogeneous material:

$$\mathbf{K} = \begin{Bmatrix} K_{\mathrm{II}} \\ K_{\mathrm{I}} \\ K_{\mathrm{III}} \end{Bmatrix} = \lim_{r\to 0}\sqrt{2\pi r}\,\boldsymbol{\Lambda}\left\langle\!\!\left\langle \left(\frac{r}{l_k}\right)^{-i\varepsilon_\alpha} \right\rangle\!\!\right\rangle \boldsymbol{\Lambda}^{-1}\begin{Bmatrix} \sigma_{12} \\ \sigma_{22} \\ \sigma_{23} \end{Bmatrix}, \tag{7}$$

$$\boldsymbol{\Lambda} = \begin{bmatrix} \lambda_1, \lambda_2, \lambda_3 \end{bmatrix} \tag{8}$$

where r is the distance from a crack tip, l_k is an arbitrary characteristic length, and the angular brackets $\langle\!\langle \ \rangle\!\rangle$ denote the diagonal matrix. λ_1, λ_2, and λ_3 are eigenvectors of the following equation:

$$\left(\mathbf{M}^* + e^{2i\pi\delta}\overline{\mathbf{M}}^*\right)\lambda = \mathbf{0}. \tag{9}$$

The explicit solution for the eigenvalues δ_α were given by Ting [14] as

$$\delta_\alpha = -\frac{1}{2} + i\varepsilon_\alpha, \quad \alpha = 1, 2, 3 \tag{10}$$

$$\varepsilon_1 = -\varepsilon, \quad \varepsilon_2 = \varepsilon = \frac{1}{2\pi}\ln\frac{1-\beta}{1+\beta}, \quad \varepsilon_3 = 0, \quad \beta = \left[-\frac{1}{2}\mathrm{tr}\left(\mathbf{WD}^{-1}\right)^2\right]^{1/2}. \tag{11}$$

In the case of a crack in a homogeneous material, each mode of the stress field is independent, and the SIFs, K_{II}, K_I, and K_{III}, are related with their respective stress fields. However, in the case of an interface crack between dissimilar anisotropic materials, each mode is related to the others, and the SIFs cannot be divided into independent modes. If both the upper and lower materials possess a symmetric plane parallel to the x_1-x_2 plane, mode III is independent while modes I and II are coupled.

The ratio between K_{II}, K_I, and K_{III} depends on the value of l_k in Equation (7). We must fix the value of l_k to relate the set of SIFs with a unique stress field. In this study, we fixed the value of l_k as 10 μm. The SIFs vector $\mathbf{K}$ for a value of l_k can easily be converted to $\mathbf{K}'$ for a different l'_k using the following relation:

$$\mathbf{K}' = \mathbf{\Lambda}\left\langle\!\!\left\langle\left(\frac{l'_k}{l_k}\right)^{i\varepsilon_\alpha}\right\rangle\!\!\right\rangle\mathbf{\Lambda}^{-1}\mathbf{K} \ . \tag{12}$$

The stress ahead of an interface crack along the x_1-axis and the crack opening displacement in the vicinity of the crack tip are expressed using the SIFs.

$$\begin{Bmatrix} \sigma_{12} \\ \sigma_{22} \\ \sigma_{23} \end{Bmatrix} = \frac{1}{\sqrt{2\pi r}}\mathbf{\Lambda}\left\langle\!\!\left\langle\left(\frac{r}{l_k}\right)^{i\varepsilon_\alpha}\right\rangle\!\!\right\rangle\mathbf{\Lambda}^{-1}\mathbf{K} \tag{13}$$

$$\begin{Bmatrix} \Delta u_1 \\ \Delta u_2 \\ \Delta u_3 \end{Bmatrix} = \sqrt{\frac{2r}{\pi}}(\overline{\mathbf{\Lambda}}^T)^{-1}\left\langle\!\!\left\langle\frac{(r/l_k)^{i\varepsilon_\alpha}}{(1+2i\varepsilon_\alpha)\cosh(\pi\varepsilon_\alpha)}\right\rangle\!\!\right\rangle\mathbf{\Lambda}^{-1}\mathbf{K} \tag{14}$$

The energy release rate G and the SIFs $\mathbf{K}$ are related as

$$G = \frac{1}{4}\mathbf{K}^T\mathbf{E}\mathbf{K}, \quad \mathbf{E} = \mathbf{D} + \mathbf{W}\mathbf{D}^{-1}\mathbf{W} \ . \tag{15}$$

In the vicinity of a crack tip, $\boldsymbol{\psi}(z)$ in Equation (3) can be simplified as

$$\boldsymbol{\psi}(z) = \mathbf{\Lambda}\left\langle\!\!\left\langle\frac{2z^{1/2+i\varepsilon_\alpha}}{1+2i\varepsilon_\alpha}\right\rangle\!\!\right\rangle\mathbf{p}_0 \tag{16}$$

$$\mathbf{p}_0 = \frac{1}{2\sqrt{2\pi}}\left\langle\!\!\left\langle\frac{e^{\pi\varepsilon_\alpha}}{l_k^{i\varepsilon_\alpha}\cosh(\pi\varepsilon_\alpha)}\right\rangle\!\!\right\rangle\mathbf{\Lambda}^{-1}\mathbf{K} \tag{17}$$

3. Numerical analyses

3.1 The M_1-integral method for the three-dimensional thermoelastic problem

The stress distribution around an interface crack tip is essentially in mixed mode. Thus, it is necessary to evaluate K_{II}, K_I and K_{III} in order to characterize the fracture behavior of a bimaterial interface crack. The distribution of stress and displacement around a crack tip in a homogeneous material is symmetric to the x_1-axis for K_I, and skew-symmetric for K_{II}. This relationship is often utilized for the mode separation of the SIFs of a crack in a homogeneous body. However, the distributions of stress and displacement around an interface crack do not have this feature. Yau and Wang [15] applied the M_1-integral, which was originally proposed by Chen and Shield [16] for a mixed mode crack problem in a homogeneous material, to bimaterial interface crack problems. Shih and Asaro [17] and Matos et al. [18] also utilized the M_1-integrals for mode separation of the SIFs of interface cracks in conjunction with the domain integral and the virtual crack extension method, respectively. The M_1-integral method for a three-dimensional thermoelastic problem is briefly explained as follows.

Several basic techniques have been developed for the numerical computation of the J-integral in a three-dimensional problem. In the present paper, the three-dimensional contour-integral method [19-21] and the domain integral method [22, 23] were employed.

We define a local orthogonal coordinate system at a point s on the crack front such as in Figure 2. The x_2 axis is perpendicular to the crack plane, and the x_1 and x_3 axes lie on the crack plane, and are normal and tangent to the crack front, respectively. Kishimoto et al. [20] defined the J-integral for a three-dimensional crack under thermal stress as

$$J = \int_\Gamma \left(W^e \delta_{1i} - \sigma_{ij} \frac{\partial u_j}{\partial x_1} \right) n_i d\Gamma + \iint_\Omega \left\{ \sigma_{ij} \alpha_{ij} \frac{\partial \vartheta}{\partial x_1} - \frac{\partial}{\partial x_3} \left(\sigma_{j3} \frac{\partial u_j}{\partial x_1} \right) \right\} d\Omega \ , \tag{18}$$

where Γ is an arbitrary contour pass on the $x_1 - x_2$ plane enclosing the crack tip in a counterclockwise direction, and Ω is the area surrounded by the contour pass. W^e is the elastic strain energy density, n_i is the x_i-component of a unit outward normal on Γ, and u_i, σ_{ij}, α_{ij} and ϑ are the displacement, stress, and coefficients of thermal expansion and temperature, respectively. Under the isothermal plane strain condition, the domain integral in Equation (18) vanishes because the partial differentiations of temperature with respect to x_1 and of displacements and stresses with respect to x_3 become zero.

Shih et al. [22] developed the domain integral method to evaluate the J-integral for three-dimensional thermoelastic cracks as

$$J = \iiint_V \left\{ -\left(W \delta_{ki} - \sigma_{ij} \frac{\partial u_j}{\partial x_k} \right) \frac{\partial q_k}{\partial x_i} + \left(\sigma_{ij} \alpha_{ij} \frac{\partial \vartheta}{\partial x_k} \right) q_k \right\} dV \bigg/ \int_{L_c} \eta(s) ds \ , \tag{19}$$

where L_c is a small segment that undergoes a virtual crack advance in the plane of the crack of a curved crack front that lies on the $x_1 - x_3$ plane (see Figure 3(a)). $\eta(s)$ is a virtual crack advance at each point s. V is a tubular domain surrounding the crack segment and bounded by the surface S_t and S_o (see Figure 3(b)). It should be noted that S_t must shrink onto the crack tip in order to evaluate the pointwise value of the J-integral along the crack front. q_k is a test function which is continuously differentiable in V, and it takes the following values on S_t and S_0:

$$q_k = \begin{cases} \eta(s)\xi_k(s) & \text{on } S_t \\ 0 & \text{on } S_o \end{cases},$$ (20)

where $\xi_k(s)$ is the x_k-component of the crack advance vector. In the present work, we can assume that the crack front in the vicinity of the crack tip is straight locally, because the sizes of finite elements around the crack tip were significantly smaller than those in the outer area. Therefore, Equation (19) is expressed as follows:

$$J = \iiint_V \left\{ -\left(W\delta_{1i} - \sigma_{ij} \frac{\partial u_j}{\partial x_1} \right) \frac{\partial q_1}{\partial x_i} + \left(\sigma_{ij} \alpha_{ij} \frac{\partial \vartheta}{\partial x_1} \right) q_1 \right\} dV \bigg/ \int_{L_c} \eta(s) ds .$$ (21)

Consider two independent equilibrium states with field variables denoted by superscripts (1) and (2) for a region surrounding a crack tip as shown in Figure 4. Superscript (1) indicates the "target problem" that we are trying to solve, and superscript (2) indicates the "reference problem" whose distributions of displacement, stress, and whose SIFs are already known. The superposition of the two equilibrium states leads to another equilibrium state, the "Superposed problem," denoted by the superscript (1+2). The distributions of displacement, stress and temperature in the superposed problem are obtained by the superposition of these two equilibrium states, (1) and (2), i.e.,

$$\begin{cases} u_i^{(1+2)} = u_i^{(1)} + u_i^{(2)} \\ \sigma_{ij}^{(1+2)} = \sigma_{ij}^{(1)} + \sigma_{ij}^{(2)} \\ \vartheta^{(1+2)} = \vartheta^{(1)} + \vartheta^{(2)} \end{cases} .$$ (22)

The SIFs vector can also be superposed as

$$\mathbf{K}^{(1+2)} = \mathbf{K}^{(1)} + \mathbf{K}^{(2)} .$$ (23)

Substituting Equation (23) into Equation (15), the energy release rate of the superposed state (1+2) is obtained as

$$J^{(1+2)} = \frac{1}{4} \left\{ \mathbf{K}^{(1)} + \mathbf{K}^{(2)} \right\}^T \mathbf{E} \left\{ \mathbf{K}^{(1)} + \mathbf{K}^{(2)} \right\} = J^{(1)} + J^{(2)} + \frac{1}{4} \left\{ \mathbf{K}^{(1)T} \mathbf{E} \mathbf{K}^{(2)} + \mathbf{K}^{(2)T} \mathbf{E} \mathbf{K}^{(1)} \right\} .$$ (24)

Hence,

$$\frac{1}{4}\left\{\mathbf{K}^{(1)T}\mathbf{E}\mathbf{K}^{(2)} + \mathbf{K}^{(2)T}\mathbf{E}\mathbf{K}^{(1)}\right\} = J^{(1+2)} - J^{(1)} - J^{(2)} = M_1 \ . \tag{25}$$

Any known problem can be used as the reference problem. The asymptotic solutions shown in Equations (1), (3), (16) and (17) can be the most convenient reference problem, and were used in this study. The M_1-integral corresponding to Equations (18) and (21) are expressed as follows:

$$
\begin{aligned}
M_1 = \int_\Gamma &\left\{\sigma_{jk}^{(1)}\varepsilon_{jk}^{(2)}\delta_{1i} - \sigma_{ij}^{(1)}\frac{\partial u_j^{(2)}}{\partial x_1} - \sigma_{ij}^{(2)}\frac{\partial u_j^{(1)}}{\partial x_1}\right\}n_i d\Gamma \\
&+ \iint_\Omega \left\{\sigma_{ij}^{(2)}\alpha_{ij}^{(1)}\frac{\partial \vartheta^{(1)}}{\partial x_1} - \frac{\partial \sigma_{j3}^{(1)}}{\partial x_3}\frac{\partial u_j^{(2)}}{\partial x_1} - \sigma_{j3}^{(2)}\frac{\partial^2 u_j^{(1)}}{\partial x_3 \partial x_1}\right\}d\Omega
\end{aligned}
\tag{26}
$$

$$
M_1 = \iiint_V \left[-\left\{\sigma_{j1}^{(1)}\varepsilon_{j1}^{(2)}\delta_{1i} - \sigma_{ij}^{(1)}\frac{\partial u_j^{(2)}}{\partial x_1} - \sigma_{ij}^{(2)}\frac{\partial u_j^{(1)}}{\partial x_1}\right\}\frac{\partial q_1}{\partial x_i} + \left\{\sigma_{ij}^{(2)}\alpha_{ij}^{(1)}\frac{\partial \vartheta^{(1)}}{\partial x_1}\right\}q_1\right]dV \bigg/ \int_{L_c} \eta(s)ds \ . \tag{27}
$$

In the present work, Equation (26) is labeled as the contour M_1-integral and Equation (27) is labeled as the domain M_1-integral. If the asymptotic solutions for (a) [$K_{\mathrm{II}}^{(2)} = 1$, $K_{\mathrm{I}}^{(2)} = 0$, $K_{\mathrm{III}}^{(2)} = 0$], (b) [$K_{\mathrm{II}}^{(2)} = 0$, $K_{\mathrm{I}}^{(2)} = 1$, $K_{\mathrm{III}}^{(2)} = 0$], and (c) [$K_{\mathrm{II}}^{(2)} = 0$, $K_{\mathrm{I}}^{(2)} = 0$, $K_{\mathrm{III}}^{(2)} = 1$] are selected, we can separate the SIFs as

$$
\begin{bmatrix} E_{11} & E_{12} & E_{13} \\ E_{21} & E_{22} & E_{23} \\ E_{31} & E_{32} & E_{33} \end{bmatrix}
\begin{Bmatrix} K_{\mathrm{II}}^{(1)} \\ K_{\mathrm{I}}^{(1)} \\ K_{\mathrm{III}}^{(1)} \end{Bmatrix} = 2\begin{Bmatrix} M_1^{(a)} \\ M_1^{(b)} \\ M_1^{(c)} \end{Bmatrix} \ . \tag{28}
$$

where E_{ij} are components of matrix $\mathbf{E}$ defined in equation (15).

3.2 Moving least-squares approximations [24]

We used moving least-squares approximation to calculate the J-integral and the M_1-integral. In the example shown in Figure 5, stress and strain used for the path integral are approximated from nodal displacements, obtained by finite element analysis. Therefore, the presented M-integral needs no elemental information from the finite element analysis. The approximation of displacement $\mathbf{u}^h(x)$ at an arbitrary point x can be written as follows:

$$\mathbf{u}^h(x) = \mathbf{p}^T(x)\mathbf{a}(x) \tag{29}$$

$$\mathbf{p}(x) = \{1,\ x,\ y,\ z\}^T \ . \tag{30}$$

$\mathbf{a}(x)$ is determined by minimizing the following weighted least-square form:

$$R(x) = \sum_I^n w(x - x_I)\left[\mathbf{p}^T(x_I)\mathbf{a}(x) - \mathbf{u}_I\right]^2 , \tag{31}$$

7

where $\mathbf{u}_I$ is the displacement at node I as shown in shown in Figure 6. The following exponential weight function was employed in this paper:

$$w(d_I) = \begin{cases} \dfrac{\exp\left(-(d_I/c)^2\right) - \exp\left(-(d_{mI}/c)^2\right)}{1 - \exp\left(-(d_{mI}/c)^2\right)}, & \text{if } d_I \leq d_{mI} \\ 0, & \text{if } d_I > d_{mI} \end{cases}, \tag{32}$$

where $d_I = \parallel x - x_I \parallel$ and $c = \beta\, d_{mI}$, and β is a parameter which determines the sharpness of the weight function. The stationary of R in Equation (31) with respect to $\mathbf{a}(x)$ is

$$\frac{\partial R}{\partial \mathbf{a}} = \sum_I^n 2w(x - x_I)\mathbf{p}(x_I)\left(\mathbf{p}^T(x_I)\mathbf{a}(x) - \mathbf{u}_I\right) = 0. \tag{33}$$

Equation (33) leads to the following form:

$$\mathbf{X}(x)\mathbf{a}(x) = \mathbf{Y}(x)\mathbf{u} \quad \text{or} \quad \mathbf{a}(x) = \mathbf{X}^{-1}(x)\mathbf{Y}(x)\mathbf{u}, \tag{34}$$

where $\mathbf{X}(x)$ and $\mathbf{Y}(x)$ are defined by

$$\begin{aligned} \mathbf{X}(x) &= \sum_I^n w(x - x_I)\mathbf{p}(x_I)\mathbf{p}^T(x_I) \\ \mathbf{Y}(x) &= \left[w(x - x_1)\mathbf{p}(x_1), w(x - x_2)\mathbf{p}(x_2), \; ... \; w(x - x_n)\mathbf{p}(x_n) \right] \end{aligned} \tag{35}$$

Substituting Equation (34) into Equation (29), we obtain

$$\mathbf{u}^h = \sum_I^n \sum_j^m p_j(x)\left[\mathbf{X}^{-1}(x)\mathbf{Y}(x)\right]_{jI}\mathbf{u}_I \equiv \sum_I^n \phi_I(x)\mathbf{u}_I, \tag{36}$$

where the shape function is given by

$$\phi_I(x) = \sum_j^m p_j(x)\left[\mathbf{X}^{-1}(x)\mathbf{Y}(x)\right]_{jI}. \tag{37}$$

Strain and stress can be calculated using the following derivative of the shape function from nodal displacements obtained by the finite element analysis.

$$\phi_{I,i} = \sum_j^m p_j\left\{ p_{j,i}\left(\mathbf{X}^{-1}\mathbf{Y}\right)_{jI} + p_j\left(\mathbf{X}_{,i}^{-1}\mathbf{Y} + \mathbf{X}^{-1}\mathbf{Y}_{,i}\right)_{jI} \right\} \tag{38}$$

4. Numerical results

The accuracy of the presented method was examined for several typical three-dimensional

interface crack problems. For all the analyses presented here, thermoelastic analyses were carried out using the MSC.Marc™ finite element program. Twenty-noded isoparametric hexahedral elements were used. No singular elements around a crack tip were used in these analyses.

4.1 Double edge cracks in jointed dissimilar isotropic plates under uniform cooling

As a benchmark, double edge cracks in jointed dissimilar isotropic semi-infinite plates subjected to a uniform change of temperature ($\Delta \vartheta = - 20°C$), as shown in Figure 7, were analyzed. This model satisfies a plane strain condition because the nodal displacements on the *X-Y* planes of the surface of the specimen are constraint for the *Z* direction. The exact solution of the SIFs is shown as the following equation [25, 26]:

$$K_{\mathrm{I}} + iK_{\mathrm{II}} = \frac{4\mu_1\mu_2\cosh(\pi\varepsilon)}{\mu_1 + \kappa_2\mu_1 +_1 \kappa_1\mu_2 + \mu_2}(\alpha_1\eta_1 - \alpha_2\eta_2)\vartheta\sqrt{\pi a}(2\varepsilon - i) \qquad \text{for} \quad l_k = 2b., \tag{39}$$

where $\kappa_j = 3 - 4v_j$, $\eta_j = 1 + v_j$ for the plane strain condition, and μ_j and α_j are the shear modulus and the coefficient of linear thermal expansion for material *j*.

The Young's moduli and Poisson's ratio were set to be $E_1 = 150$ GPa, $E_2 = 20$ GPa and $v_1 = 0.30$, $v_2 = 0.25$, respectively. The corresponding bimaterial constant is $\varepsilon = -0.08552$. The coefficients of linear thermal expansion were $\alpha_1 = 3.0\mathrm{x}\ 10^{-6}$ (1/°C) and $\alpha_2 = 1.0\mathrm{x}\ 10^{-4}$ (1/°C), respectively, and the change of temperature ϑ was $- 20°C$. The exact solutions of the SIFs for $l_k = 2b$ obtained by equation (39) were converted to the SIFs for $l_k = 10\mu m$ using equation (12). The converted SIFs for $l_k = 10\mu m$ are $K_{\mathrm{II}} = -3.78$ ($\mathrm{MPa}\sqrt{\mathrm{m}}$) and $K_{\mathrm{I}} = 1.97(\mathrm{MPa}\sqrt{\mathrm{m}})$. Due to the symmetries of the geometry and thermal loading, a half model was analyzed as shown in Figure 7. The numbers of nodes and elements of the finite element mesh, whose smallest element size, *m*, around a crack tip was 1/20 of the ligament length *b*, were 280,309 and 66,150, respectively. The ligament length $2b$ was 20 mm.

In this study, three different types of test functions q_1 for the domain *J*-integral and the domain M_1-integral were examined. The first is (a) a Bilinear function defined as

$$q_1(r,x_3) = \begin{cases} \left(1 - \dfrac{|x_3|}{L_c/2}\right) & 0 < r \le r_1 \\[4mm] \left(1 - \dfrac{|x_3|}{L_c/2}\right)\left(\dfrac{r_2 - r}{r_2 - r_1}\right) & r_1 < r \le r_2 \end{cases}, \tag{40}$$

where *r* is the distance from the crack tip on the $x_1 - x_2$ plane. r_2 is the radius of the integration domain, and r_1 is an arbitrary radius within the range $0 \le r_1 < r_2$, as shown in Figure 3(b). q_1 is the continuous function that varies bilinearly in the *r* direction, and varies linearly in the x_3 direction

9

(see Figure 8(a)). This function q_1 is constant within the range r from 0 to r_1 for the constant x_3, and so $\partial q_1/\partial r = 0$. The second type of test function q_1 is (b) a Quadratic function, which is defined to vary quadratically in the r and the x_3 directions, as shown in the following equation (see Figure 8(b)):

$$q_1(r,x_3) = \left\{1 - \left(\frac{x_3}{L_c/2}\right)^2\right\}\left\{1 - \left(\frac{r}{r_2}\right)^2\right\}. \tag{41}$$

The third is (c) a Bilinear-Quadratic function defined as

$$q_1(r,x_3) = \begin{cases} \left\{1 - \left(\dfrac{x_3}{L_c/2}\right)^2\right\} & 0 < r \le r_1 \\[2em] \left\{1 - \left(\dfrac{x_3}{L_c/2}\right)^2\right\}\left(\dfrac{r_2 - r}{r_2 - r_1}\right) & r_1 < r \le r_2 \end{cases}, \tag{42}$$

where q_1 is a continuous function that varies bilinearly in the r direction, and varies quadratically in the x_3 direction.

The energy release rate G at the center of the plate thickness (see Figure 7) was calculated by the domain J-integral using the three types of test functions q_1, (a) the Bilinear function, (b) the Quadratic function and (c) the Bilinear-Quadratic function, whose integral domains were selected such that the segment L_c was equal to the length of an element allocated at the crack tip; $L_c/m = 1.0$, and the r_1 took a value in the range of zero through three times the length of an element; $r_1/m = 0.0$, 1.0, 2.0 and 3.0.

The relationships between errors and the domain radii r_2 are shown in Figures 9 (a)-(c). In Figures 9 (a) and (c), when the domain radii r_2 are more than $r_2/m = 4.0$ and $r_1/m = 1.0$, 2.0, and 3.0, the results show good path-independency and accuracy within 2%. On the other hand, the results obtained under the condition $r_1/m = 0.0$ were much worse than others. Figure 9 (b) shows the good path-independency and accuracy within 2% when the domain radii r_2 are more than $r_2/m = 2.5$. We examined the effect of the segment length L_c on the results under the condition $r_1/m = 2.0$, as shown in Figure 10. There was a little difference in accuracy between the results obtained by $L_c/m = 1.0$ and those obtained by $L_c/m = 2.0$. If the crack front is curved, the length of the segment L_c cannot be made longer due to the assumption of a locally straight crack front.

The energy release rate G at the center of the plate thickness was also obtained using the contour J-integral. In order to check the path independency, the contour J-integral was calculated using several paths by varying the radius of the integral path. The relationship between the rate of error

and the path radius is shown in Figure 11. When the radius of the integral path is more than $r/m = 2.0$, which is equal to two times the length of an element at the crack tip, the results show good path-independency within about 2.0% accuracy.

We evaluated the SIFs along the crack front using the contour M_1-integral and the domain M_1-integral, as shown in Figure 12. The contour M_1-integral was calculated selecting $r/m = 4.0$ as the integral path, and the domain M_1-integral was calculated with a (a) Bilinear function q_1 whose integral domain was set as $r_1/m = 2.0$, $r_2/m = 4.0$ and $L_c/m = 2.0$. The relative errors of the numerical results obtained by the present methods based on the analytical solution were defined as

$$Error_i = \frac{K_i - K_{i\,|\,exact}}{\sqrt{K_{II\,|\,exact}^2 + K_{I\,|\,exact}^2 + K_{III\,|\,exact}^2}} \quad (\,i = \text{I, II, III}\,)\,, \tag{43}$$

where $Error_i$ is the relative error (%), and $K_{i\,|\,exact}$ is the analytical solution of the SIFs.

Figure 12 shows that there is little difference between the accuracy of SIFs obtained by the contour M_1-integral and that obtained by the domain M_1-integral. Both methods were able to provide accuracies within 1.1%. The error of K_{II} was larger than those of K_I and K_{III}, because K_{II} is the dominant mode in the thermoelastic problem.

4.2 An external circular interface crack between dissimilar anisotropic materials under thermal load

We next analyzed an external circular interface crack between dissimilar anisotropic materials, as shown in Figure 13. Two different boundary conditions were examined, the uniform change of temperature (Sample 1, $\vartheta = -20°C$) and the uniform gradient of temperature with respect to X (Sample 2: $\partial\vartheta/\partial X = -0.1°C/mm$). The material properties of the anisotropic materials are shown in Table 1. In these tables, Aragonite and Topaz are orthotropic materials, and LT and GSO are monoclinic materials. The combinations of materials are described in Table 2. Utilizing the symmetries of the geometry, thermal loading and material properties, a half body was modeled.

We performed thermoelastic analyses using three sets of finite element meshes with different fineness, as shown in Table 3. The size of the smallest elements of Meshes 1 – 3 were 1/20, 1/40 and 1/80 of the half ligament length b, respectively. Because we could not find the exact solutions for these problems, the convergences of the numerical solutions were examined. The energy release rate and SIFs at $\varphi = 22.5°$, $90°$, $157.5°$ of the crack front as shown in Figure 13 were calculated by the contour M_1-integral and the domain M_1-integral, and they are shown in Tables 4 – 9. The domain M_1-integral was calculated with a Bilinear function q_1 whose integral domain was set as $r_1/m = 2.0$, $r_2/m = 4.0$ and $L_c/m = 2.0$. In these tables, as the meshes become finer, the obtained energy release

rate and SIFs converge towards constant values. There was little difference between the results calculated by the contour M_1-integral and those calculated by the domain M_1-integral. In the combination of LT and GSO, K_I at $\varphi = 90°$ is a negative value, which indicates that two crack surfaces overlap over a relatively large area. This phenomenon is mathematically correct but physically incorrect. If we use the SIFs as the fracture criteria in our future study, we need to consider the effect of this overlap. However, in this study we focused on the numerical techniques to obtain the SIFs of the traditional asymptotic solution, which allows that stress oscillates and the two crack surfaces overlap. The asymptotic solution of stress distributions ahead of the crack tip along the interface and crack opening displacements (COD), which were obtained by substituting the SIFs analyzed by the contour M_1-integral using Mesh 1 into Equations (13) and (14), were compared with those obtained by the finite element method using Mesh 3, as shown in Figures 14 – 21. These figures show results of the following two material combinations. One is Case a (Aragonite and Topaz). Figures 14 and 15 show the Sample 1 and Figures 18 and 19 show the Sample 2, respectively. Another is Case c (LT and GSO). Figures 16 and 17 show the Sample 1 and Figures 20 and 21 show the Sample 2, respectively. The asymptotic solutions of stress and the COD are in excellent agreement with the distributions obtained by the finite element analyses, except σ_{23} and Δu_3 at $\varphi = 90°$ and σ_{22} at $\varphi = 22.5°$, $90°$, and $157.5°$. In the case when the asymptotic solutions are in disagreement with the finite element results, K_I and K_{III}, which are strongly related to σ_{22}, Δu_2, and σ_{23}, Δu_3, respectively, are relatively small values compared with the other modes of SIFs. It is necessary to use a very fine mesh to accurately analyze SIFs with such small values.

In Figures 22 and 23, the distributions of SIFs along the crack front obtained by the contour M_1-integral using Mesh 1 are demonstrated. As shown in these figures, K_{II} and K_{III} are the dominant modes of SIFs in the thermoelastic problem and show complicated variations along the crack fronts due to the effect of elastic anisotropy.

5. Conclusions

A numerical method is proposed for evaluating the stress intensity factors of a three-dimensional interfacial crack between general anisotropic bimaterials subjected to thermal stress. In this paper, the three-dimensional thermal contour-integral method and the three-dimensional thermal domain-integral method were examined to calculate the J-integral and the M_1-integral of interfacial cracks in a three-dimensional body under thermal stress. The moving least-square approximation was utilized to calculate the value of the J-integral and the M_1-integral. The M_1-integral in conjunction with the moving least-square approximation can calculate the stress intensity factors from the nodal displacements obtained by the finite element analysis. The present methods were

initially applied to double edge interfacial cracks in jointed dissimilar isotropic semi-infinite plates under uniform cooling. The results obtained by the present methods showed excellent agreement with the analytical solutions. Thermoelastic analyses of external circular interface cracks between jointed dissimilar anisotropic materials subjected to a uniform change of temperature and to a uniform gradient of temperature were also performed. The convergence of the energy release rate and the stress intensity factors calculated by the present methods was examined using several finite element meshes which possess different fineness. In the vicinity of an interfacial crack tip, the asymptotic solutions of stress and the COD obtained by the stress intensity factors were in good agreement with those obtained directly by the finite element analysis with a very fine mesh. These facts indirectly prove that the results obtained by the presented methods are reasonable.

References

1. Gotoh, M., Some problems of Bonded Anisotropic Plates with Cracks along the Bond, *International Journal of Fracture Mechanics*, Vol. 3, 253-265 (1967).

2. Clements, D. L., A Crack between Dissimilar Anisotropic Media, *International Journal of Engineering Science*, Vol. 9, 257-265 (1971).

3. Willis, J. R., Fracture Mechanics of Interfacial Cracks, *Journal of the Mechanics and Physics of Solids*, Vol. 19, 353-368 (1971).

4. Bassani, J. R. and Qu, J., Finite Crack on Bimaterial and Bicrystal Interface, *Journal of the Mechanics and Physics of Solids*, Vol. 37, 435-453 (1971).

5. Wu, K. C., Stress Intensity Factor and Energy Release Rate for Interfacial Crack between Dissimilar Anisotropic Materials, *Transactions of the ASME Journal of Applied Mechanics*, Vol. 57, 882-886 (1990).

6. Hwu. C., Fracture Parameters for The Orthotropic Bimaterial Interface Cracks, Engineering Fracture Mechanics, Vol. 45, 89-97 (1993).

7. Stroh, A. N., Steady State Problems in Anisotropic Elasticity, *Journal of Mathematics and Physics*, Vol. 41, 77-103 (1962).

8. Sun, C. T. and Qian, W., The use of Finite Extension Strain Energy Release Rates In Fracture of Interfacial Cracks, *International Journal of Solids and Structures*, Vol. 34, 2595-2609 (1997).

9. Ikeda, T., Nagai, M., Yamanaga, K. and Miyazaki, N., Stress Intensity Factors Analysis of an Interface Crack between Anisotropic Dissimilar Materials using the Finite Element Method, *Engineering Fracture Mechanics*, Vol. 73, 2067-2079 (2006).

10. Nomura, Y. Ikeda, T. and Miyazaki, N., Stress Intensity Factor Analysis at an Interfacial Corner between Anisotropic Bimaterials under Thermal Stress, Engineering Fracture Mechanics, Vol. 76,

221-233, 2009.

11. Nagai, M., Ikeda, T. and Miyazaki, N., Stress Intensity Factor Analysis of an Interface Crack between Dissimilar Anisotropic Materials under Thermal Stress using the Finite Element Analysis, *International Journal of Fracture*, Vol. 146, 233-248, 2007.

12. Nagai, M., Ikeda, T. and Miyazaki, N., Stress Intensity Factors Analysis of a Three-Dimensional Interface Crack between Dissimilar Anisotropic Materials, *Engineering Fracture Mechanics*, Vol. 74, 2481-2497, 2007.

13. Barnett, D. M. and Lothe, J., Synthesis of the Sextic and the Integral Formalism for Dislocations, Greens Function and Surface Waves in Anisotropic Elastic Solids, *Physicanorvegica*, Vol. 7 13-19 (1973).

14. Ting, T. C. T., Explicit Solution and Invariance of the singularities at an interface crack in anisotropic composites, *International Journal of Solids and Structures*, Vol. 22, 965-983 (1986).

15. Yau, J. F. and Wang S. S., An analysis of interface cracks between dissimilar isotropic materials using conservation integrals in elasticity, *Engineering Fracture Mechanics*, Vol 20, 423-432 (1984).

16. Chen, F. H. K. and Shield R. T., Conservation laws in elasticity of the J-integral type, *Journal of Applied Mathematics and Physics (ZAMP)*, Vol. 28, 1-22 (1977).

17. Shih, C. F. and Asaro R.J., Elastic-plastic analysis of cracks on bimaterial interfaces: part I-small scale yielding, *Transactions of the ASME Journal of Applied Mechanics*, Vol. 55, 299-316 (1988).

18. Matos, P. P. L , McMeeking R. M., Charalambides P. G. and Drory M. D., A method for calculating stress intensities in bimaterial fracture, *International Journal of Fracture*, Vol. 40, 235-254 (1989).

19. Miyamoto, H. and Kikuchi M., Three-dimensional J Integral, *Theoretical and Applied Mechanics*, Vol. 28, 195-204 (1980).

20. Kishimoto K, Aoki S. and Sakata M., On the path independent integral-J^, *Engineering Fracture Mechanics*, Vol. 13, 841-850 (1980).

21. Amestoy M, Bui H. D. and Labbens R., On the definition of local path independent integrals in three-dimensional crack problems, *Mechanic Research Communications*, Vol. 8, 231-236 (1981).

22. Shih C. F., Moran B. and Nakamura T., Energy release rate along a three-dimensional crack front in a thermally stressed body, *International Journal of Fracture*, Vol. 30, 79-102 (1986).

23. Nikishkov G. P. and Atluri S. N., Calculation of fracture mechanics parameters for an arbitrary three-dimensional crack, by the 'Equivalent Domain Integral' method, *International Journal for Numerical Methods in Engineering*, Vol. 24, 1801-1821 (1987).

24. Lancaster P. and Salkauskas K., Surface Generated by Moving Least Squares Methods, *Mathematics of Computation*, Vol. 37, 141-158 (1981).

25. Erdogan F., Stress Distribution in Bonded Dissimilar Materials with Cracks, *Transactions of the ASME Journal of Applied Mechanics*, Vol. 32, 403-410 (1963).

26. Ikeda T and Sun C. T., Stress Intensity Factor Analysis for An Interface Crack between Dissimilar Isotropic Materials under Thermal Stress, *International Journal of Fracture*, Vol. 111, 229-249 (2001).

Table(s)

Table 1 Elastic stiffnesses C_{ij} (GPa) and CTE ($\times 10^{-6}$/K) used in the thermoelastic analyses.

Elastic Stiffnesses	Aragonite (Orthotropic)	Topaz (Orthotropic)	LT (Trigonal)	GSO (Monoclinic)
C_{11}	159	281	230	223
C_{12}	36.6	126	42	108
C_{13}	1.97	84.6	79	98.5
C_{15}	0	0	11	84
C_{22}	87	349	$= C_{11}$	150
C_{23}	15.9	88.2	$= C_{13}$	102
C_{25}	0	0	$= -C_{15}$	33.3
C_{33}	85	295	275	251
C_{35}	0	0	0	−6
C_{44}	41.3	108	96	78.8
C_{46}	0	0	$= C_{15}$	6.6
C_{55}	25.6	133	$= C_{44}$	68.8
C_{66}	42.7	131	$= (C_{11} - C_{12})/2$	82.7
α_{11}	35.0	5.9	16.1	4.4
α_{22}	17.0	4.8	16.1	14.0
α_{33}	10.0	4.4	4.1	6.8
α_{31}	0	0	0	−1.4

Table 2 Combinations of anisotropic materials used in the thermoelastic analyses.

	Material 1	Material 2
Case *a*	Aragonite	Topaz
Case *b*	Aragonite	GSO
Case *c*	LT	GSO

Table 3 Finite element meshes for the analyses of an external circular interface crack under thermal load.

	Number of nodes	Number of elements	m/b
Mesh 1	246,487	58,432	0.05
Mesh 2	474,851	114,00	0.025
Mesh 3	685,529	165,840	0.0125

m: size of the smallest element around a crack tip.

Table 4 Calculated stress intensity factors of an external circular interface crack for Sample 1 (Aragonite-Topaz).

φ (degree)	Mesh	G (10^2 J/m^2)		K_{II} (MPa m$^{1/2}$)		K_{I} (MPa m$^{1/2}$)		K_{III} (MPa m$^{1/2}$)	
		Contour	Domain	Contour	Domain	Contour	Domain	Contour	Domain
	Mesh 1	1.40	1.41	4.31	4.33	1.35	1.37	0.97	0.98
22.5	Mesh 2	1.39	1.40	4.31	4.33	1.36	1.37	0.97	0.98
	Mesh 3	1.39	1.40	4.33	4.35	1.35	1.36	0.97	0.97
	Mesh 1	0.37	0.37	2.07	2.09	0.88	0.92	-	-
90.0	Mesh 2	0.36	0.36	2.08	2.09	0.90	0.92	-	-
	Mesh 3	0.37	0.37	2.09	2.10	0.91	0.91	-	-
	Mesh 1	1.40	1.41	4.31	4.33	1.35	1.37	−0.97	−0.98
157.5	Mesh 2	1.39	1.40	4.31	4.33	1.36	1.37	−0.97	−0.98
	Mesh 3	1.39	1.40	4.33	4.35	1.35	1.36	−0.97	−0.97

Table 5 Calculated stress intensity factors of an external circular interface crack for Sample 1 (Aragonite-GSO).

φ (degree)	Mesh	G (10^2 J/m^2)		K_{II} (MPa m$^{1/2}$)		K_I (MPa m$^{1/2}$)		K_{III} (MPa m$^{1/2}$)	
		Contour	Domain	Contour	Domain	Contour	Domain	Contour	Domain
	Mesh 1	1.26	1.27	3.79	3.80	1.03	1.03	1.21	1.22
22.5	Mesh 2	1.25	1.25	3.78	3.78	1.02	1.02	1.20	1.20
	Mesh 3	1.26	1.26	3.79	3.80	1.02	1.01	1.20	1.19
	Mesh 1	0.07	0.06	0.73	0.76	0.22	0.26	−0.02	−0.03
90.0	Mesh 2	0.06	0.06	0.75	0.77	0.24	0.26	−0.03	−0.04
	Mesh 3	0.06	0.06	0.75	0.78	0.24	0.26	−0.03	−0.04
	Mesh 1	1.23	1.24	3.62	3.64	0.97	0.97	−1.33	−1.35
157.5	Mesh 2	1.22	1.23	3.64	3.64	0.98	0.98	−1.33	−1.34
	Mesh 3	1.22	1.23	3.65	3.67	0.97	0.98	−1.33	−1.33

Table 6 Calculated stress intensity factors of an external circular interface crack for Sample 1 (LT-GSO).

φ (degree)	Mesh	G (J/m^2)		K_{II} (MPa m$^{1/2}$)		K_I (MPa m$^{1/2}$)		K_{III} (MPa m$^{1/2}$)	
		Contour	Domain	Contour	Domain	Contour	Domain	Contour	Domain
	Mesh 1	28.5	28.7	2.37	2.37	0.05	0.05	0.61	0.62
22.5	Mesh 2	28.7	28.7	2.35	2.35	0.04	0.04	0.60	0.61
	Mesh 3	28.9	28.9	2.35	2.35	0.04	0.04	0.60	0.60
	Mesh 1	2.69	2.38	0.61	0.64	−0.03	−0.02	−0.02	−0.03
90.0	Mesh 2	2.49	2.40	0.63	0.64	−0.03	−0.02	−0.04	−0.05
	Mesh 3	2.45	2.42	0.64	0.65	−0.03	−0.02	−0.06	−0.06
	Mesh 1	27.7	27.8	2.15	2.17	0.01	0.02	−0.72	−0.74
157.5	Mesh 2	27.6	27.6	2.18	2.19	0.02	0.02	−0.73	−0.74
	Mesh 3	27.5	27.7	2.19	2.21	0.02	0.02	−0.74	−0.74

Table 7 Calculated stress intensity factors of an external circular interface crack for Sample 2 (Aragonite-Topaz).

φ (degree)	Mesh	G (J/m^2)		K_{II} (MPa m$^{1/2}$)		K_I (MPa m$^{1/2}$)		K_{III} (MPa m$^{1/2}$)	
		Contour	Domain	Contour	Domain	Contour	Domain	Contour	Domain
	Mesh 1	38.7	39.0	2.27	2.28	0.71	0.72	0.49	0.50
22.5	Mesh 2	38.4	38.6	2.27	2.28	0.71	0.72	0.49	0.49
	Mesh 3	38.4	38.7	2.28	2.29	0.71	0.71	0.49	0.49
	Mesh 1	9.22	9.19	1.03	1.05	0.44	0.46	−0.07	−0.07
90.0	Mesh 2	9.13	9.13	1.04	1.04	0.45	0.46	−0.07	−0.07
	Mesh 3	9.17	9.18	1.05	1.05	0.46	0.46	−0.07	−0.07
	Mesh 1	31.5	31.8	2.04	2.05	0.64	0.65	−0.48	−0.49
157.5	Mesh 2	31.4	31.5	2.04	2.05	0.65	0.65	−0.48	−0.49
	Mesh 3	31.4	31.6	2.05	2.06	0.64	0.65	−0.48	−0.48

Table 8 Calculated stress intensity factors of an external circular interface crack for Sample 2 (Aragonite-GSO).

φ (degree)	Mesh	G (J/m^2)		K_{II} (MPa m$^{1/2}$)		K_I (MPa m$^{1/2}$)		K_{III} (MPa m$^{1/2}$)	
		Contour	Domain	Contour	Domain	Contour	Domain	Contour	Domain
	Mesh 1	34.5	34.8	1.99	1.99	0.53	0.53	0.63	0.63
22.5	Mesh 2	34.3	34.4	1.98	1.98	0.53	0.53	0.62	0.63
	Mesh 3	34.4	34.4	1.99	1.99	0.53	0.53	0.62	0.62
	Mesh 1	1.78	1.53	0.36	0.38	0.11	0.13	−0.05	−0.05
90.0	Mesh 2	1.58	1.52	0.37	0.38	0.12	0.13	−0.06	−0.06
	Mesh 3	1.53	1.53	0.38	0.39	0.12	0.13	−0.06	−0.06
	Mesh 1	28.1	28.2	1.73	1.73	0.46	0.46	−0.64	−0.65
157.5	Mesh 2	27.8	27.9	1.73	1.74	0.46	0.46	−0.64	−0.64
	Mesh 3	27.8	28.0	1.73	1.75	0.46	0.46	−0.64	−0.64

Table 9 Calculated stress intensity factors of an external circular interface crack for Sample 2 (LT-GSO).

φ (degree)	Mesh	G (J/m^2)		K_{II} (MPa m$^{1/2}$)		K_{I} (MPa m$^{1/2}$)		K_{III} (MPa m$^{1/2}$)	
		Contour	Domain	Contour	Domain	Contour	Domain	Contour	Domain
	Mesh 1	7.84	7.87	1.24	1.25	0.02	0.02	0.32	0.32
22.5	Mesh 2	7.88	7.88	1.24	1.23	0.02	0.01	0.31	0.31
	Mesh 3	7.91	7.92	1.24	1.23	0.01	0.01	0.31	0.31
	Mesh 1	0.73	0.64	0.30	0.32	–0.01	–0.01	–0.04	–0.04
90.0	Mesh 2	0.65	0.62	0.31	0.32	–0.01	–0.01	–0.05	–0.05
	Mesh 3	0.63	0.62	0.31	0.32	–0.01	–0.01	–0.05	–0.06
	Mesh 1	6.27	6.31	1.03	1.04	–0.01	0.01	–0.35	–0.36
157.5	Mesh 2	6.26	6.26	1.04	1.04	0.01	0.01	–0.35	–0.36
	Mesh 3	6.25	6.30	1.04	1.05	0.01	0.01	–0.36	–0.36
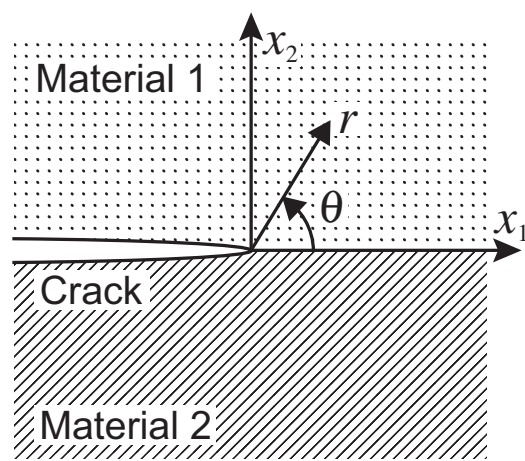
Figure 1 An interfacial crack between dissimilar anisotropic materials.
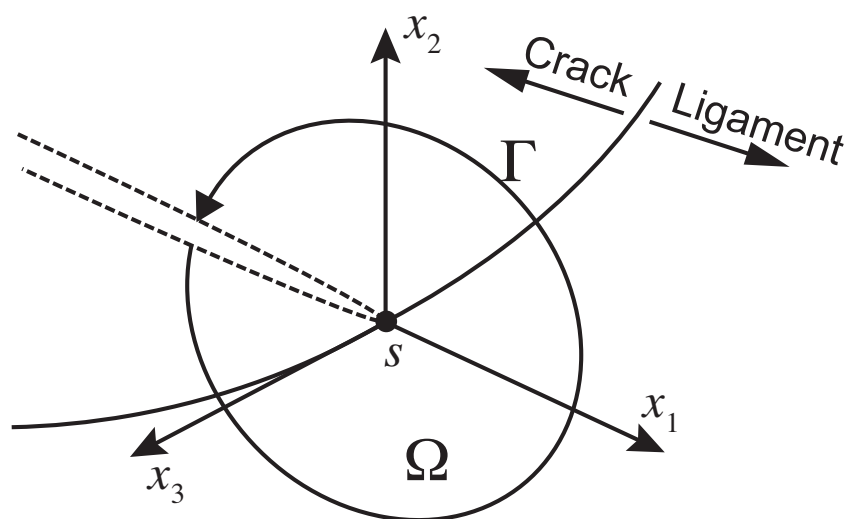
Figure 2 Schematic of the *J*-integral in a three-dimensional crack.
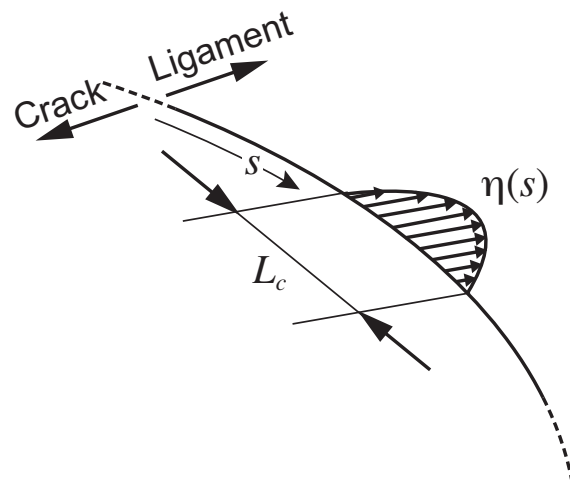
(a) A small segment of a crack front that undergoes a virtual crack advance.
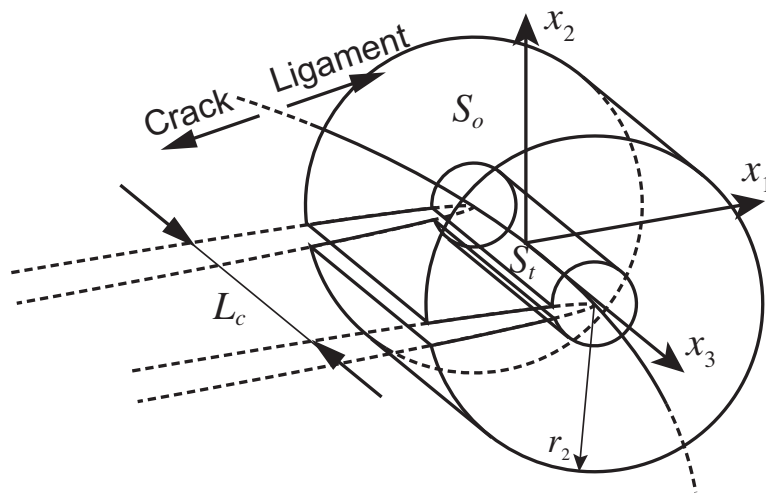
(b) The tubular domain surrounding a segment of a crack front.

Figure 3 Schematic of the domain integral in a three-dimensional crack.
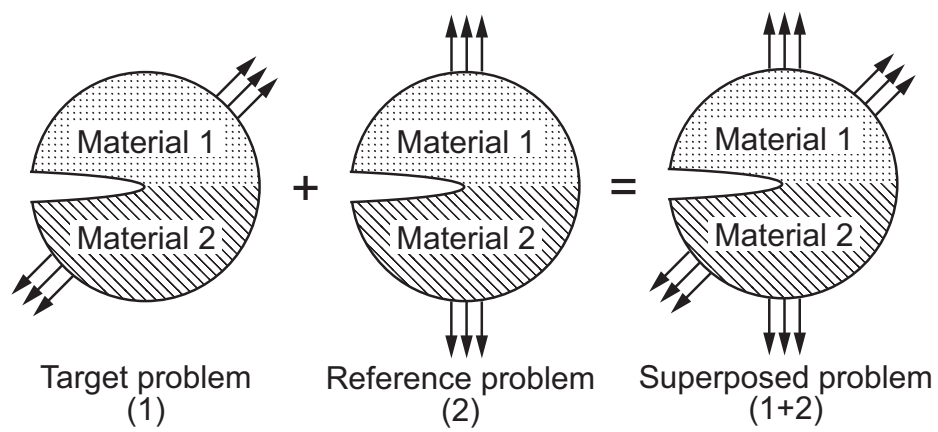
Figure 4 The concept of the superposition of a reference problem onto a target problem.
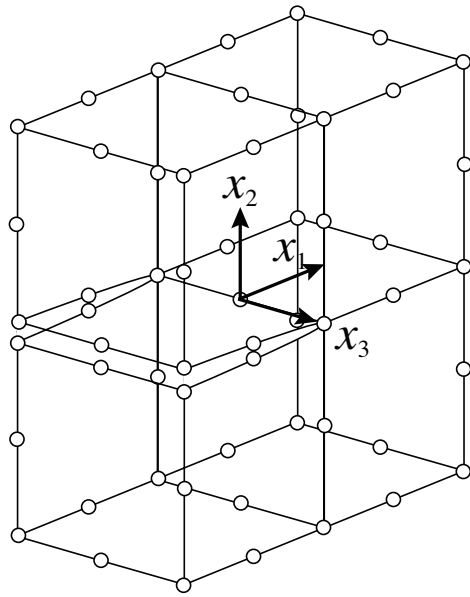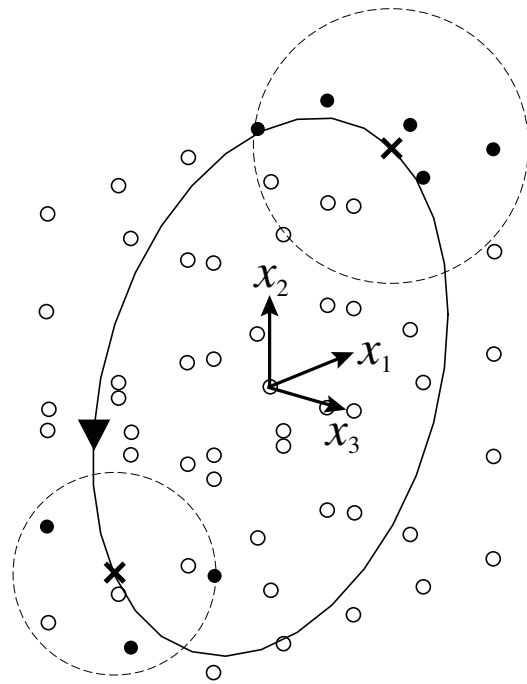
Finite element meshes   Path integral

Figure 5 Three-dimensional contour integral using moving least-square approximation.
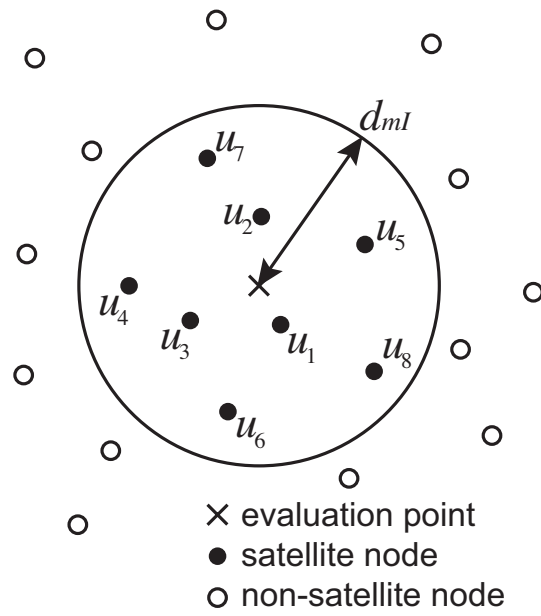
Figure 6 The influence domain for the moving least-square approximation.
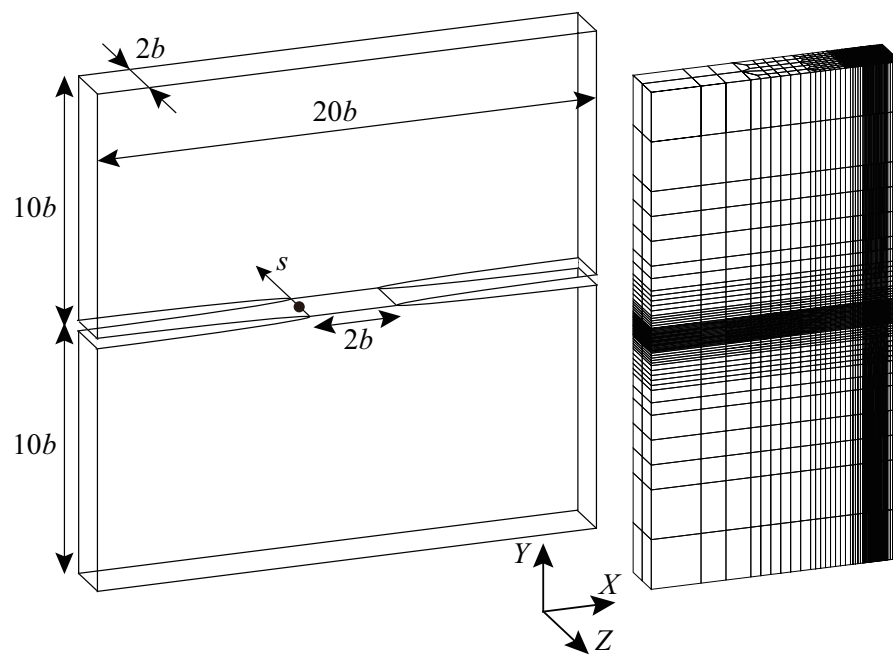
Figure 7 Double edge cracks in jointed dissimilar isotropic plates under uniform cooling.
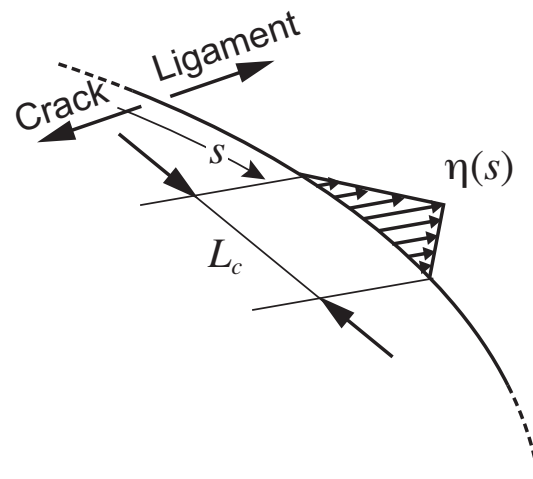
(a) Linear
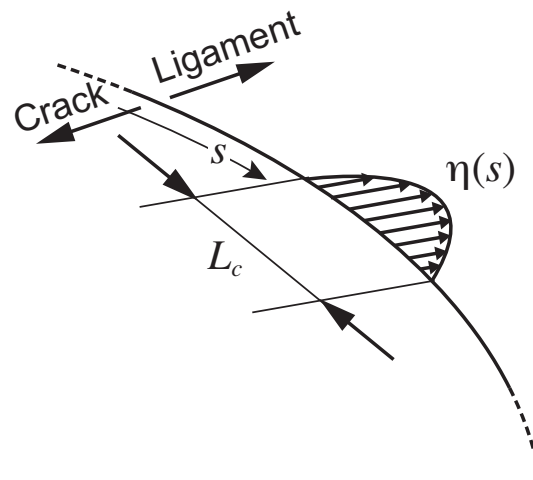
(b) Quadratic

Figure 8 Variations of weight function along x_3 direction of the domain J-integral.
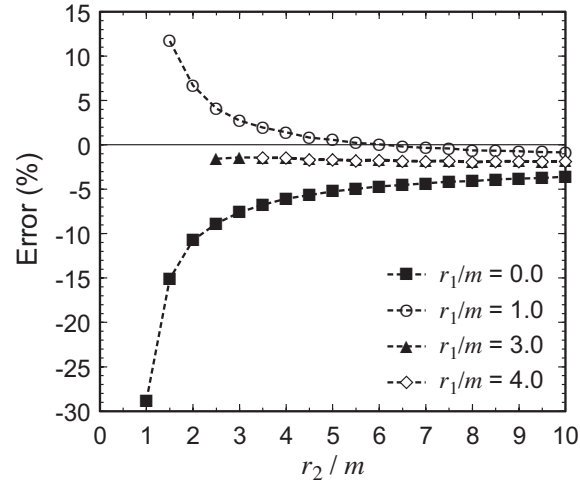
(a) Bilinear function
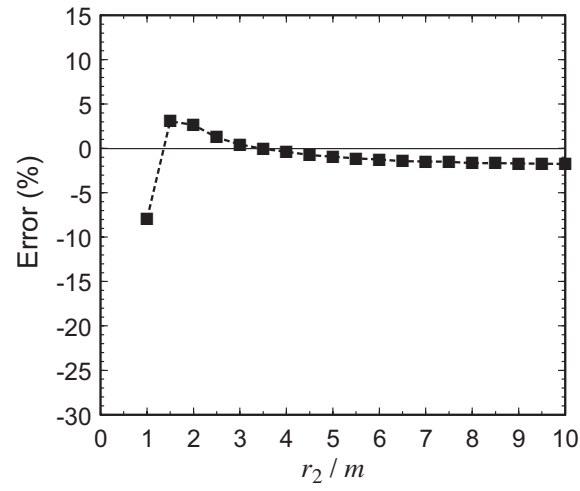
(b) Quadratic function
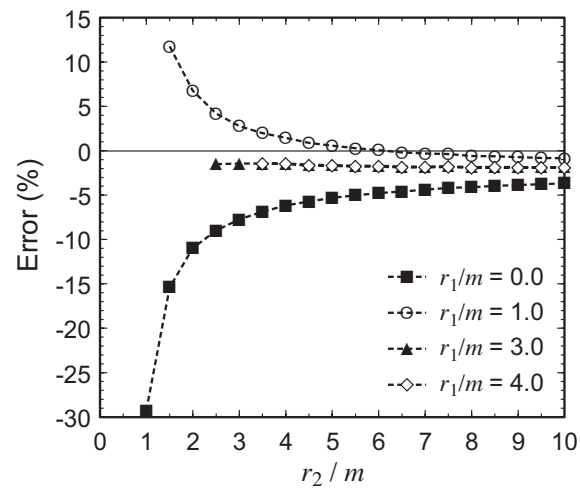
(c) Bilinear-Quadratic function

Figure 9 The relationship between errors and path radii for the domain J-integral (m: size of the smallest element around a crack tip).
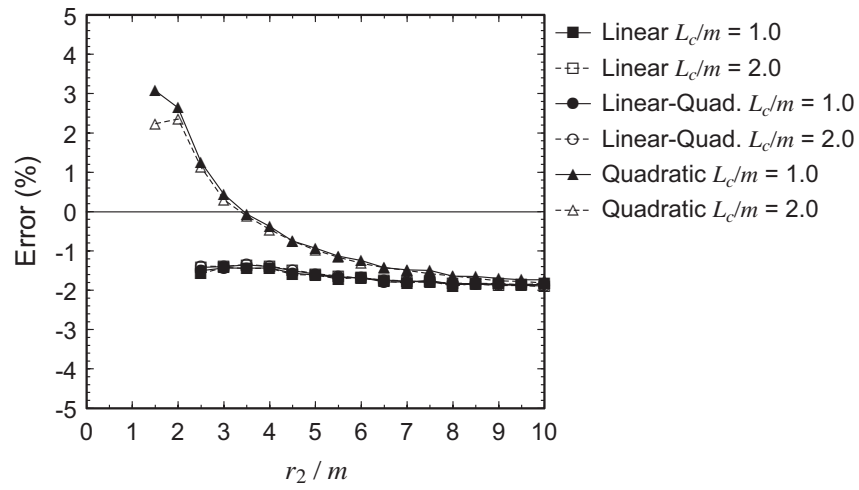
Figure 10 The relationship between errors and path radii for several segment L_c.
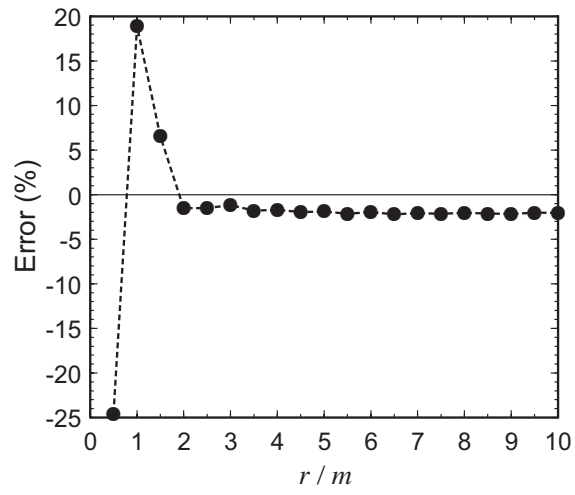
Figure 11 The relationship between errors and path radii for the contour *J*-integral (*m*: size of the smallest element around a crack tip).
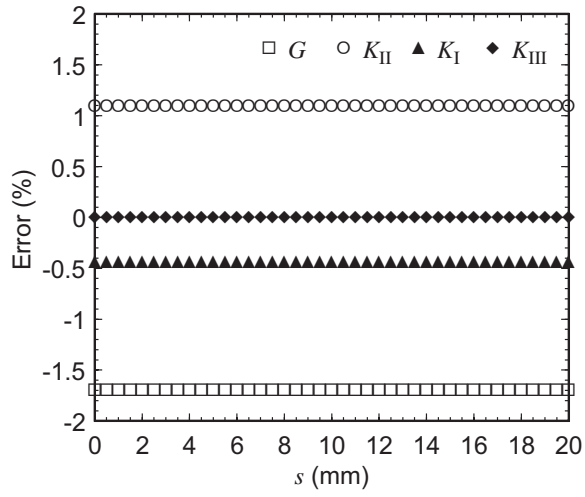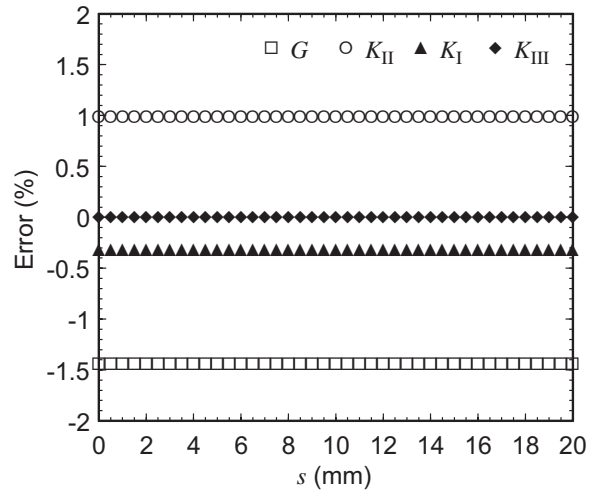
(a) Contour M_1-integral　　　　　(b) Domain M_1-integral

Figure 12 Distributions of the errors of the stress intensity factor along an interface crack in jointed dissimilar isotropic plates under uniform cooling.
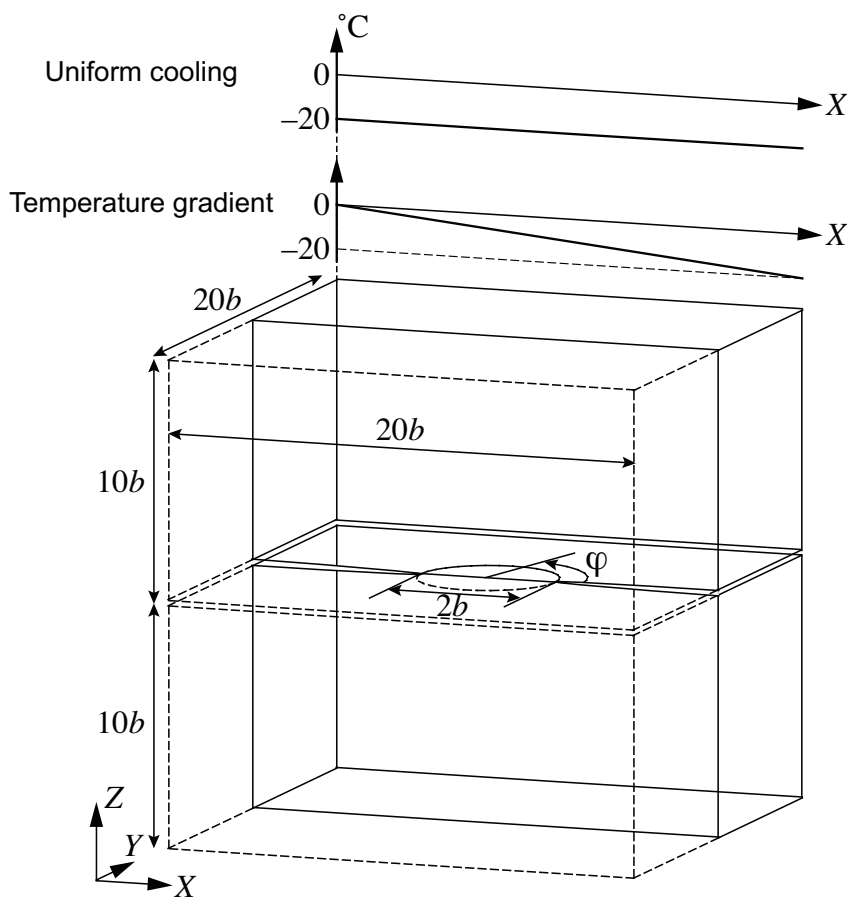
Figure 13 An external circular interface crack between dissimilar anisotropic materials under thermal load.

(a) φ = 22.5°

(b) φ = 90.0°

(c) φ = 157.5°
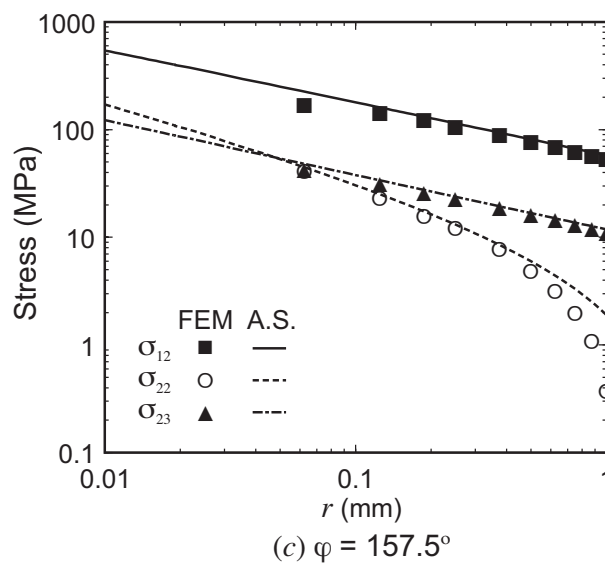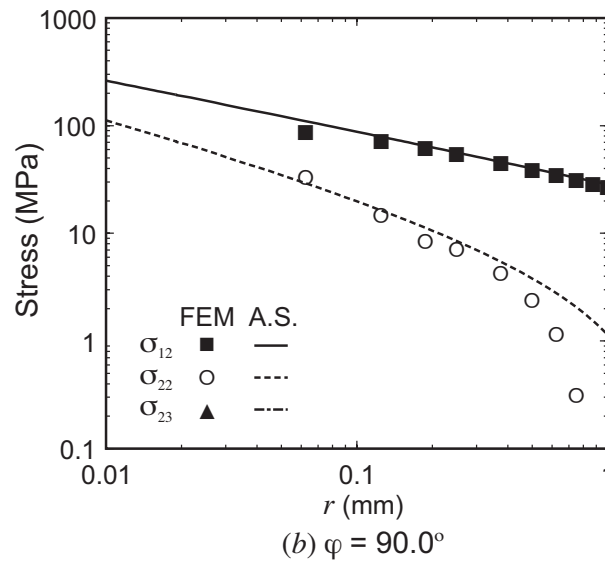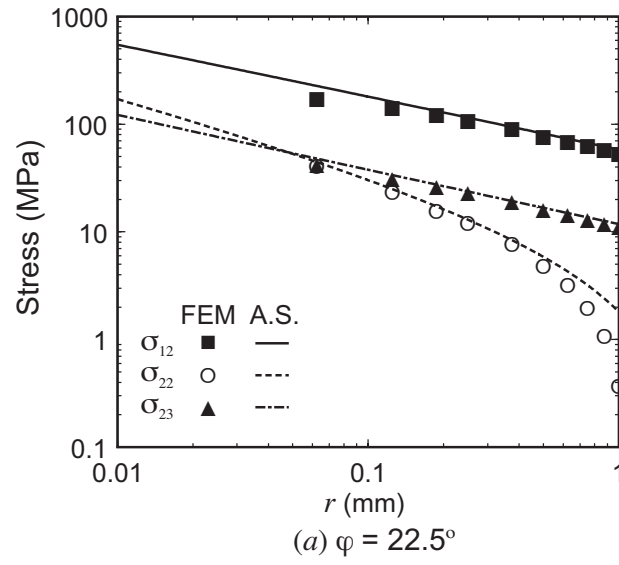
Figure 14 Asymptotic solutions of stress ahead of crack tips compared with those obtained by the FEM (Case a for Sample 1).
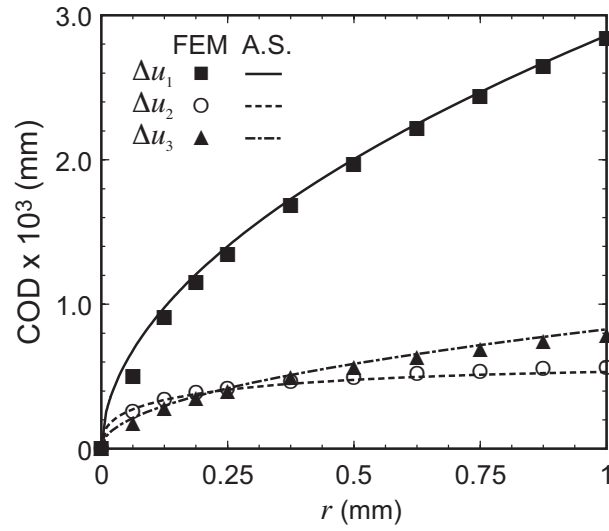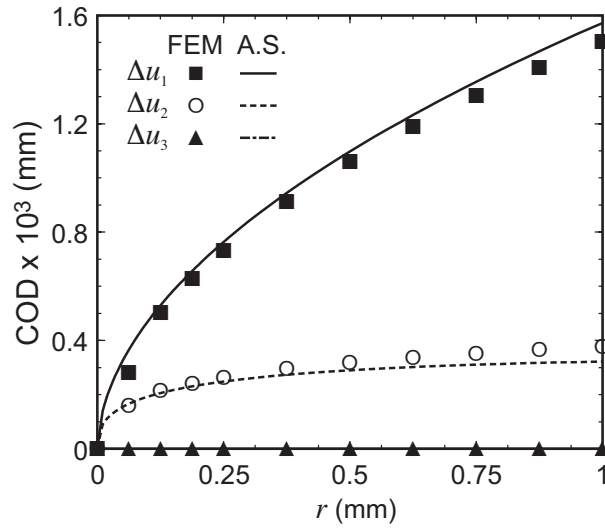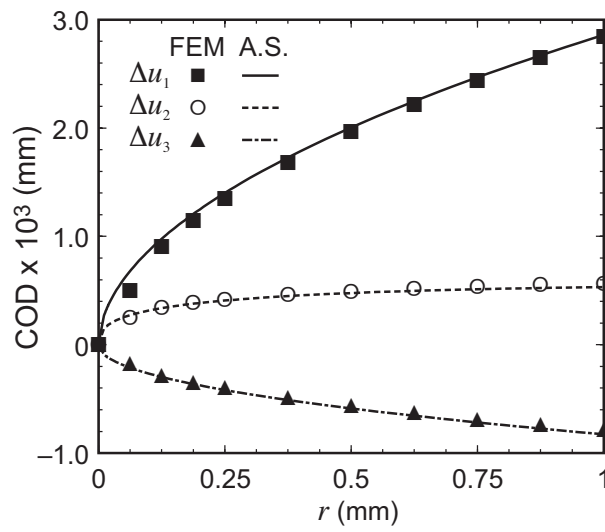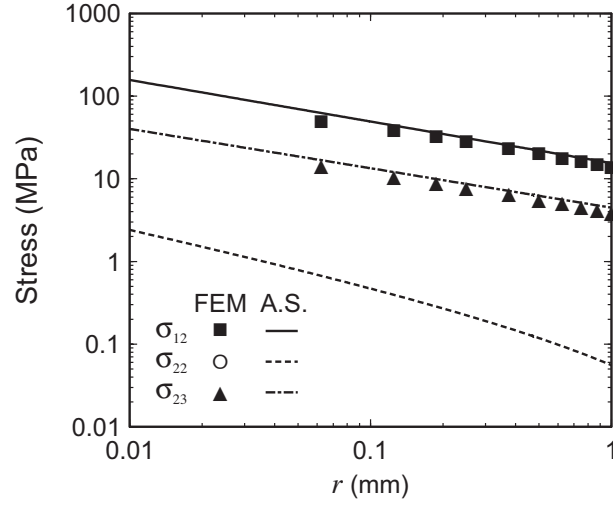
Figure 15 Asymptotic solutions of the COD compared with those obtained by the FEM (Case a for Sample 1).
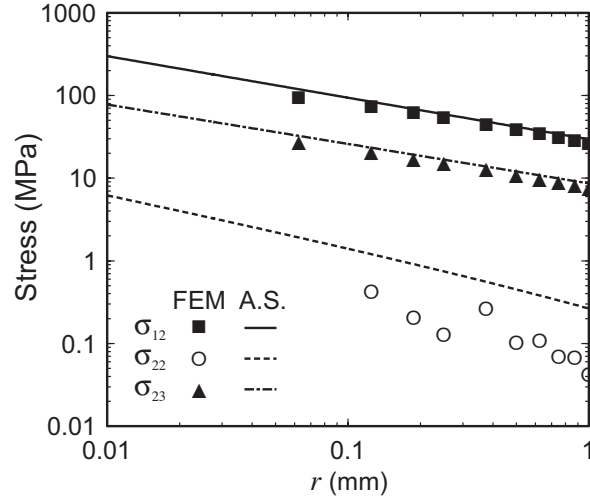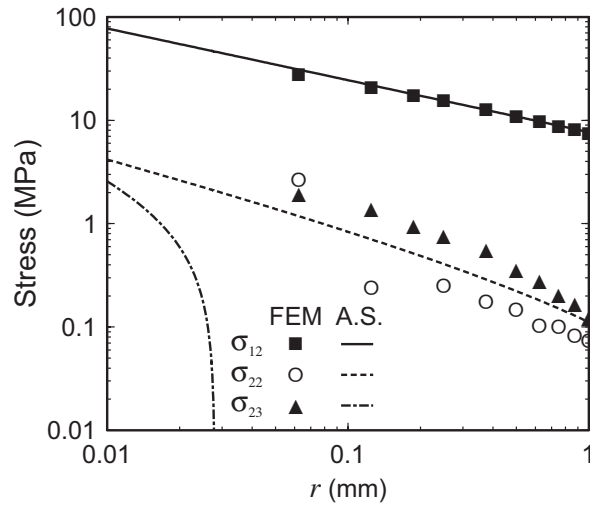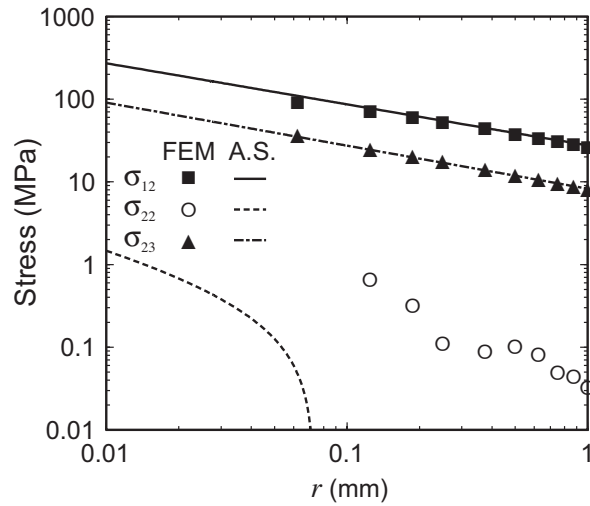
Figure 16 Asymptotic solutions of stress ahead of crack tips compared with those obtained by the FEM (Case c for Sample 1).
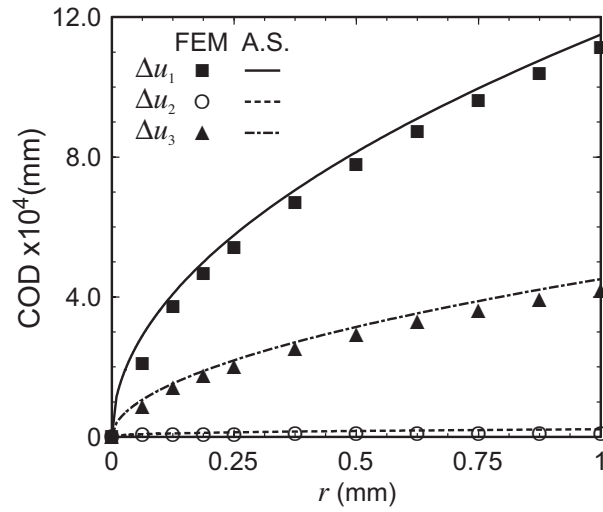
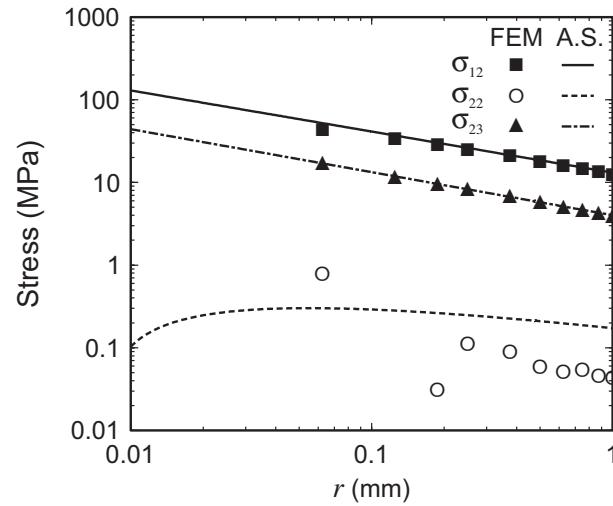(a) $\varphi = 22.5°$
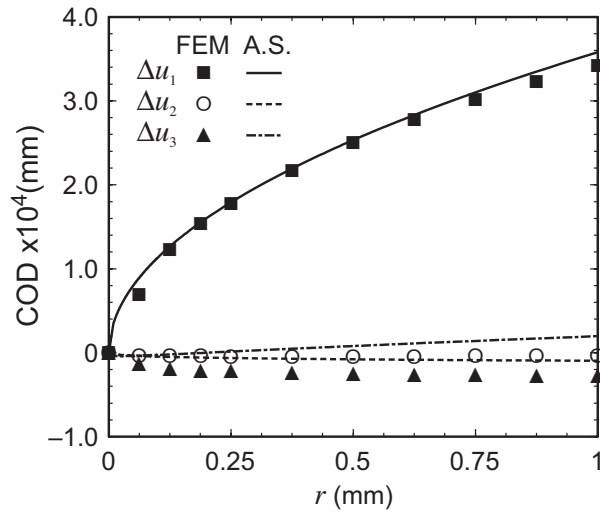
(b) $\varphi = 90.0°$
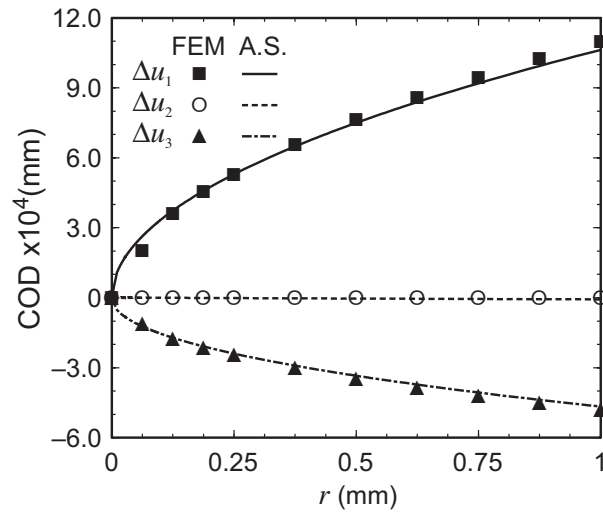
(c) $\varphi = 157.5°$

Figure 17 Asymptotic solutions of the COD compared with those obtained by the FEM (Case c for Sample 1).

(*a*) φ = 22.5°

(*b*) φ = 90.0°
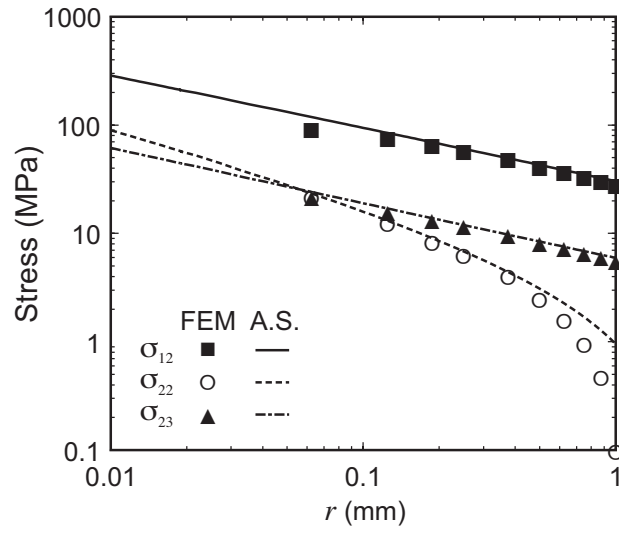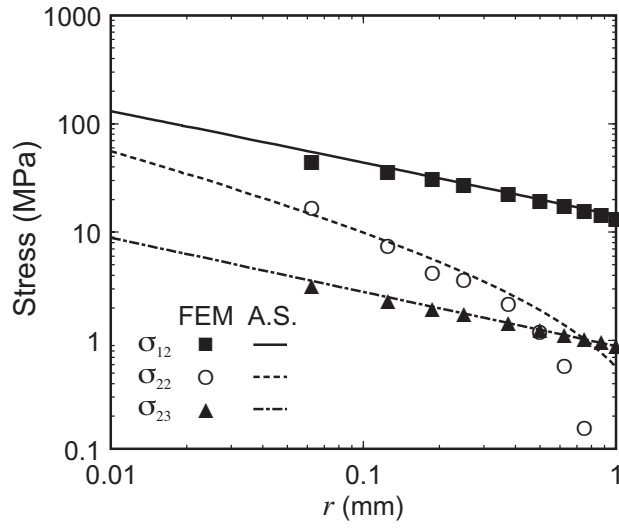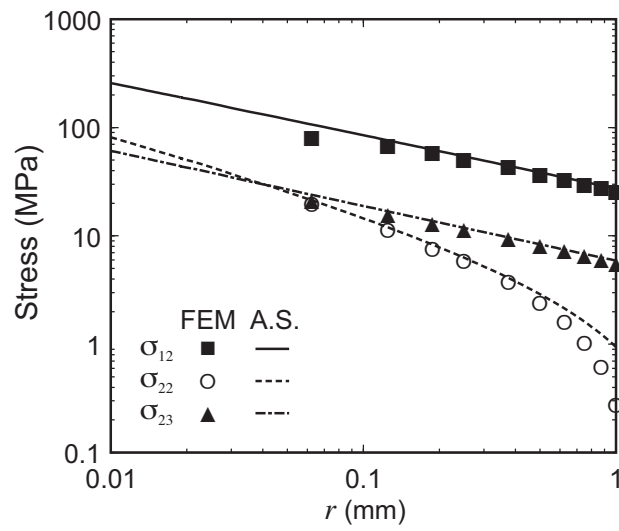
(*c*) φ = 157.5°

Figure 18 Asymptotic solutions of stress ahead of crack tips compared with those obtained by the FEM (Case a for Sample 2).

(a) φ = 22.5°

(b) φ = 90.0°
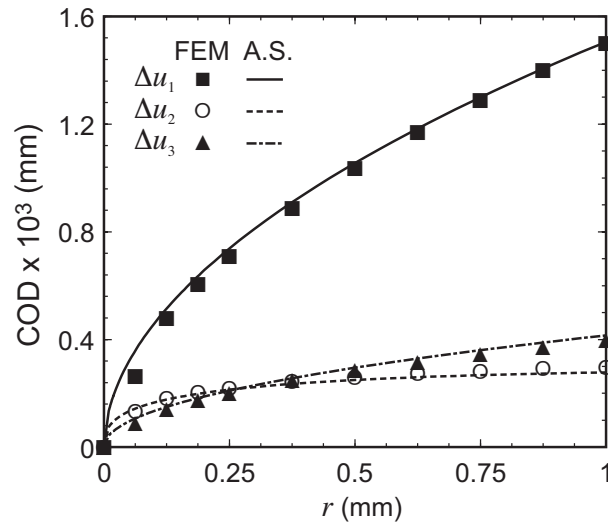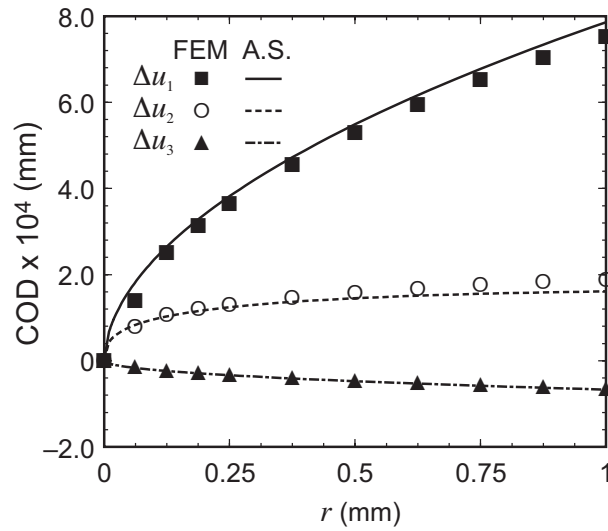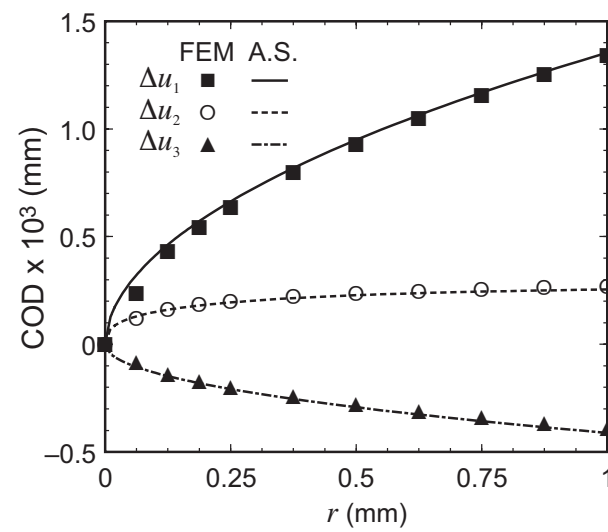
(c) φ = 157.5°

Figure 19 Asymptotic solutions of the COD compared with those obtained by the FEM (Case a for Sample 2).

(a) φ = 22.5°

(b) φ = 90.0°
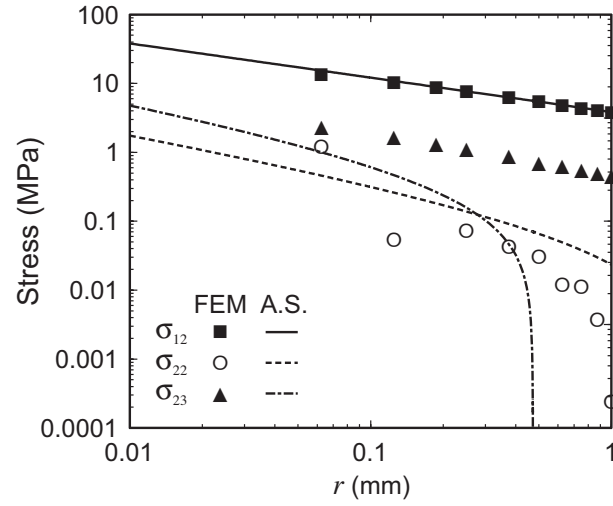
(c) φ = 157.5°

Figure 20 Asymptotic solutions of stress ahead of crack tips compared with those obtained by the FEM (Case c for Sample 2).
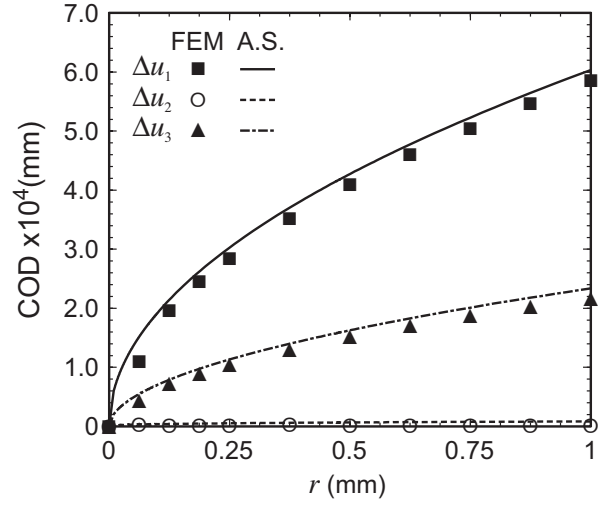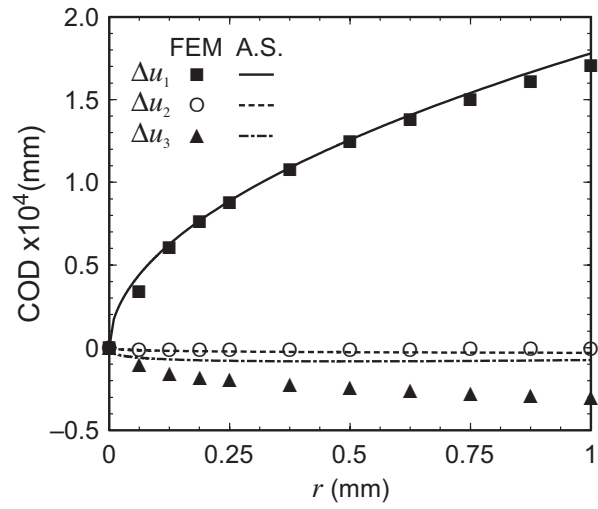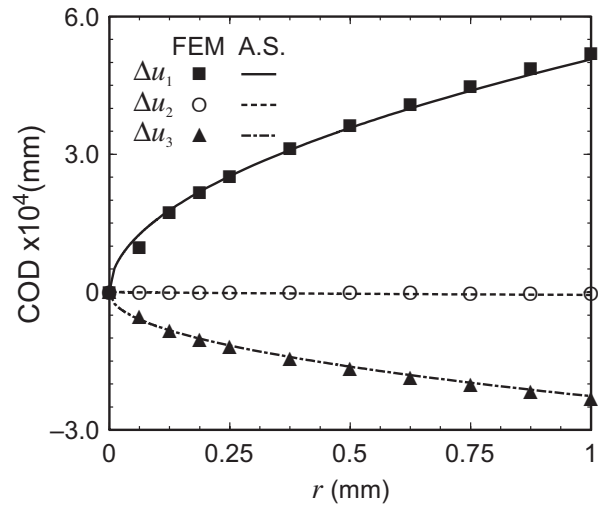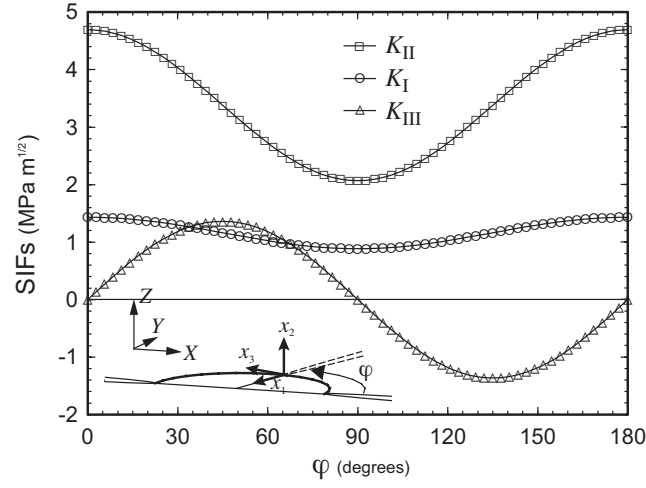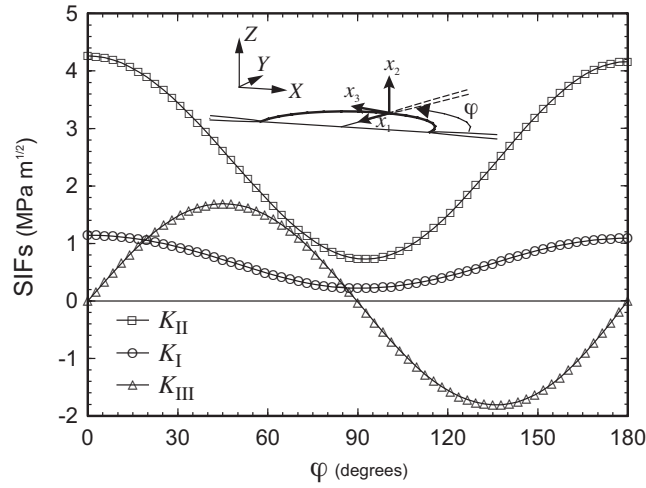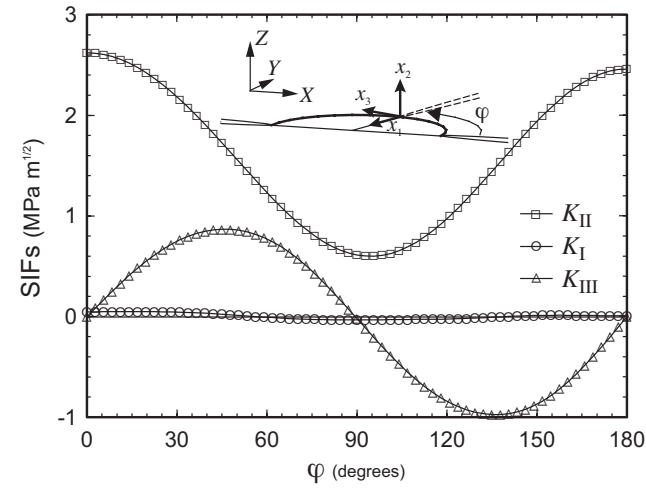
Figure 21 Asymptotic solutions of the COD compared with those obtained by the FEM (Case c for Sample 2).

(*a*) Case *a* (Aragonite/Topaz)

(*b*) Case *b* (Aragonite/GSO)

(*c*) Case *c* (LT/GSO)

Figure 22 The distributions of stress intensity factors along the crack fronts obtained by the contour M_1-integral with Mesh 1 for Sample 1.
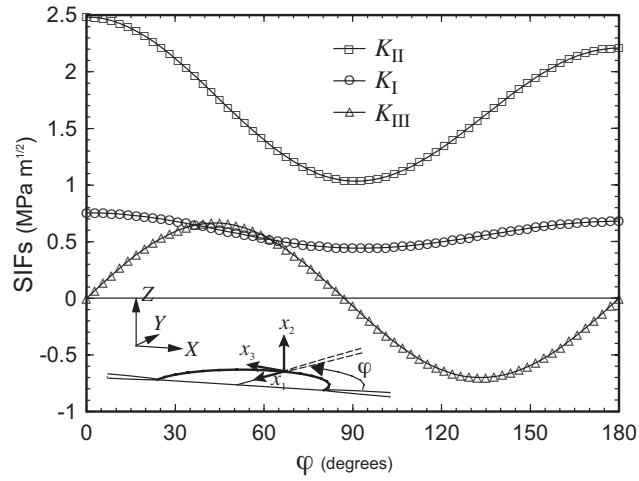
(a) Case *a* (Aragonite/Topaz)

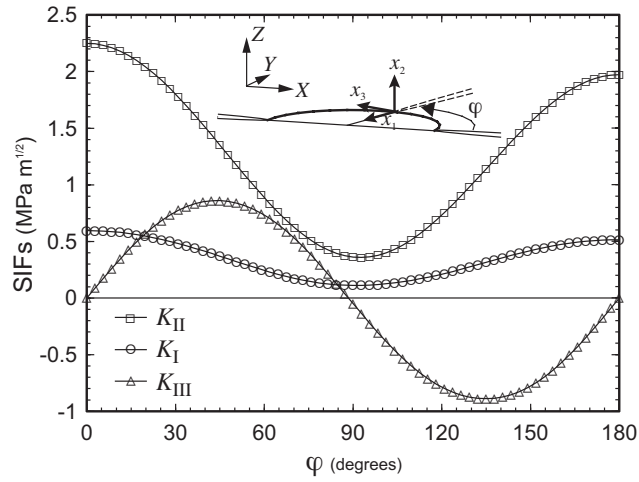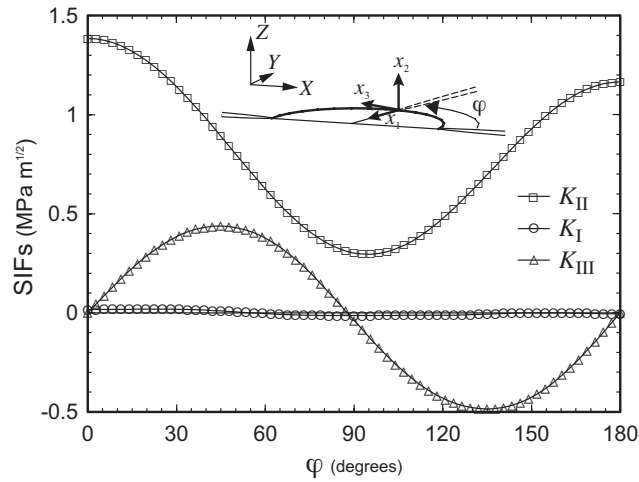(b) Case *b* (Aragonite/GSO)

(c) Case *c* (LT/GSO)

Figure 23 The distributions of stress intensity factors along the crack fronts obtained by the contour M_1-integral with Mesh 1 for Sample 2.

Nomenclatures

$\mathbf{A}$ and $\mathbf{B}$:   Stroh's eigenvectors matrices of a material

C_{ijks}:   Elastic stiffness tensors

$\mathbf{D}$ and $\mathbf{W}$:   Bi-materials constant matrices

$\mathbf{E}$:   Bi-materials constant matrix

E_{ij}:   Bi-materials constant tensors

$\mathbf{f}$:   Function vector

G: Energy release rate

J: J-integral

$\mathbf{K} = \begin{Bmatrix} K_{\mathrm{II}} \\ K_{\mathrm{I}} \\ K_{\mathrm{III}} \end{Bmatrix}$:   Stress intensity factors

$\mathbf{L}$ and $\mathbf{S}$:   Barnett-Lothe tensors

l_k :   Characteristic length

L_c :   Small segment along a crack front

$\mathbf{M}^*$:   Bi-materials matrix

n_i: Unit normal vector on the boundary

$\mathbf{N}_1$ and $\mathbf{N}_3$:   Functions of elastic constants

$\mathbf{p}$:   Linear basis

q_k $(k = 1, 2, 3)$:   Test functions

r :   Distance from the crack-tip

$\mathbf{S}$ and $\mathbf{L}$:   Barnett-Lothe tensors

S_o and S_t :   Surfaces of Tubular domain V

t_i :   Boundary tractions

$\mathbf{u}$:   Displacement vector

u_i $(i = 1, 2, 3)$:   Displacements

V: Tubular domain surrounding the crack segment

W^e: Elastic strain energy density

w: Weight function

x_i $(i=1, 2, 3)$:   Rectangular coordinate system

α_{ij} $(i = 1, 2, 3; j = 1, 2, 3)$:   Coefficients of thermal expansion tensors

δ_α $(\alpha = 1, 2, 3)$:   Eigenvalues

ε :   Oscillation index

η :   Virtual crack advance

ϕ :   Shape function

Λ: Eigenvector matrix

λ_i $(i=1, 2, 3)$:   Eignevectors

ε_{ij} $(i = 1, 2, 3; j = 1, 2, 3)$:   Elastic strain tensors

Γ: Arbitrary contour pass on the $x_1 - x_2$ plane enclosing the crack tip

μ_k: Shear modulus

σ_{ij} $(i = 1, 2, 3; j = 1, 2, 3)$:   Stress tensor

ϑ :   Temperature

ξ_k $(k = 1, 2, 3)$:   Crack advanced vectors

Ω: Area surrounded by the contour pass Γ

ψ: Stress function